IOP Publishing Plasma Physics and Controlled Fusion

Plasma Phys. Control. Fusion **57** (2015) 115003 (29pp) doi:10.1088/0741-3335/57/11/115003

# Physics-based control-oriented modeling and robust feedback control of the plasma safety factor profile and stored energy dynamics in ITER

**Justin E Barton[1], Karim Besseghir[2], Jo Lister[2] and Eugenio Schuster[1]**

[1] Department of Mechanical Engineering and Mechanics, Lehigh University, 19 Memorial Drive West, Bethlehem, PA 18015, USA
[2] École Polytechnique Fédérale de Lausanne (EPFL), Centre de Recherches en Physique des Plasmas (CRPP), Association EURATOM-Suisse, 1015 Lausanne, Switzerland

E-mail: justin.barton@alum.lehigh.edu

Received 20 January 2015, revised 22 July 2015
Accepted for publication 6 August 2015
Published 10 September 2015


**Abstract**

Many challenging plasma control problems still need to be addressed in order for the ITER plasma control system (PCS) to be able to maintain the plasma within a predefined operational space and optimize the plasma state evolution in the tokamak, which will greatly aid in the successful achievement of ITER's goals. Firstly in this work, a general control-oriented, physics-based modeling approach is developed to obtain *first-principles-driven* (FPD) models of the plasma magnetic profile and stored energy evolutions valid for high performance, high confinement (H-mode) scenarios, with the goal of developing model-based closed-loop algorithms to control the safety factor profile ($q$ profile) and stored energy evolutions in the tokamak. The FPD model is tailored to H-mode burning plasma scenarios in ITER by employing the DINA-CH & CRONOS free-boundary tokamak simulation code, and the FPD model's prediction capabilities are demonstrated by comparing the prediction to data obtained from DINA-CH & CRONOS. Secondly, a model-based feedback control algorithm is designed to simultaneously track target $q$ profile and stored energy evolutions in H-mode burning plasma scenarios in ITER by embedding the developed FPD model of the magnetic profile evolution into the control design process. The feedback controller is designed to ensure that the closed-loop system is *robust* to uncertainties in the electron density, electron temperature and plasma resistivity, and is tested in simulations with the developed FPD model. The effectiveness of the controller is demonstrated by first tracking nominal $q$ profile and stored energy target evolutions, and then modulating the generated fusion power while maintaining the $q$ profile in a stationary condition. In the process, many key practical issues for plasma profile control in ITER are investigated, which will be useful for the development of the ITER PCS that has recently been initiated. Some of the more pertinent investigated issues are the time necessary to drive the $q$ profile and stored energy to a target evolution, and whether plasma control can be achieved through the use of separate individual control algorithms or whether a more fully integrated approach is required.

Keywords: plasma control, advanced scenarios control, physics-model-based control, safety factor profile control

(Some figures may appear in colour only in the online journal)

 

## 1. Introduction

The successful achievement of ITER's goals greatly relies on the ability of the ITER plasma control system (PCS) to maintain the plasma state in a predefined operational space ensuring stability and safety limits are not violated, stabilize numerous plasma instabilities, optimize the evolution of average plasma parameters and plasma profiles, avoid or mitigate plasma disruptions and be able to respond to any abnormal event requiring a change in the control action in a seamless fashion. This will require the development of optimized, yet robust, algorithms that can coordinate the available actuation capabilities to control multiple strongly coupled plasma parameters. Algorithms to control the plasma parameters can be developed by employing either non-model-based or model-based control techniques. Most likely, non-model-based single-input-single-output (SISO) control loops will not be able to satisfy the plasma profile control performance requirements needed for ITER because the SISO control loops cannot account for the multiple effects a given actuator has on the plasma evolution. Additionally, non-model-based controllers require trial-and-error tuning and are not conducive to developing integrated algorithms to control coupled plasma parameters, which may require coordinated actuator sharing. Both of these characteristics are impractical for use on ITER. Model-based control is motivated by the coupled, nonlinear, multivariable, distributed parameter dynamics of the plasma. In the development of model-based controllers, the dominant physics of the system is embedded into the control design process through a multi-input-multi-output (MIMO) control-oriented dynamic model. Therefore, the developed controllers know in which direction to actuate to generate a desired response in the plasma state evolution and can be designed to share the available actuation capabilities. As a result, model-based control design inherently reduces the need for trial-and-error tuning of the algorithm and has the potential to meet the demanding control requirements of ITER.

To develop model-based controllers (control algorithms), control-oriented models that describe the plasma response to the actuators, i.e. poloidal field coil voltages, electron cyclotron heating/current-drive, etc, must first be developed. These models can be obtained by employing either data-driven or first-principles-driven (FPD) modeling techniques. Data-driven models are developed by mainly considering the response of the system output, i.e. the plasma parameters to be controlled, around a specified reference state due to modulations in the system actuators, and little if any physical understanding is incorporated into the model. As a result of the model identification process, most data-driven models are inherently linear, and are only valid around the reference plasma state adopted during the data identification process. This in turn may limit the effectiveness of controllers designed by utilizing these models when the plasma state deviates from the adopted reference state. Also, as the data-driven models are strongly dependent on system input–output data, dedicated identification experiments are needed on each device, and potentially for each operating scenario, to develop the models.

A substantial physics effort has been ongoing for several years to develop predictive models for the evolution of the magnetic and kinetic plasma profiles in toroidal plasmas, such as poloidal magnetic flux and electron temperature. The core of these first-principles models are the fundamental physical laws that govern the behavior of the plasma, such as conservation equations (mass, momentum, energy, charge) and Maxwell's equations, for instance. These physics models have been incorporated into complex simulation codes utilized to model the plasma dynamics and predict the evolution of the plasma in existing and future tokamak devices, with some examples being PTRANSP [1], ONETWO [2], CORSICA [3], ASTRA [4], DINA-CH & CRONOS [5–9] and FASTRAN [10]. The goal in developing FPD, control-oriented models is the conversion of these physics models into a form *suitable for control design*. Where first-principles knowledge of a particular plasma parameter is either too complex for control design or not fully understood, such as the plasma thermal conductivity, general physical observations, which are not unique to any one machine, and experimental/simulated data are used to close the first-principles model by developing a simplified model of the plasma parameter in question, thereby obtaining a *first-principles-driven* model. First-principles are not only based on *ab initio* modeling, but can be based on some empirical observations such as abnormal diffusivity.

It is important to note that FPD models are developed with control design in mind. Consequently, the models need only capture the dominant physics of the plasma dynamics that are relevant to the control objective since one of the main characteristics of feedback control is the ability to deal with model uncertainties, such as unmodeled dynamics that have a relatively small influence on the plasma state evolution from a control design point-of-view. It is often not possible, however, to assess the true requirements for model accuracy until experimental tests (or simulation tests based on more detailed models) of the model-based controller are performed. Therefore, an iterative process may be necessary. Additionally, FPD models have the advantages of being (i) extendable to various magnetohydrodynamic (MHD) equilibrium configurations and operating scenarios, (ii) able to incorporate the nonlinear coupling between the various plasma parameters and (iii) able to explicitly describe the temporal and spatial evolution of the plasma profiles in response to nonlinear control actuation. As these models mainly rely on fundamental physical laws, FPD models can readily be adapted to a given operating scenario in a given tokamak as preexisting experimental data from the machine of interest, or in the case of ITER simulated data from an advanced simulation code, is all that is needed to close the model. Finally, FPD modeling provides the freedom of arbitrarily handling the trade-off between the simplicity of the model and both its physics accuracy and its range of validity, which will of course be reflected in the model-based controller's performance and capability.

In order for ITER to meet its demanding performance objectives in terms of fusion power generation and long-pulse duration, extensive research has been conducted to find advanced operating scenarios [11] characterized by a high fusion gain, good plasma confinement, MHD stability and a

noninductively driven plasma current with a dominant fraction coming from the bootstrap current [12] so as to minimize the necessary amount of auxiliary current-drive needed to maintain the desired scenario [13]. A key plasma property that is investigated in the development of these scenarios is the safety factor profile ($q$ profile) because of its close relationship to plasma energy/particle transport [14, 15], which affect both the magnitudes and gradients of the plasma temperature and density profiles, and to plasma stability limits that are approached by increasing the plasma pressure [16, 17]. The temperature and density gradients are important due to their relationship to the bootstrap current, and the temperature and density profiles themselves are important due to their relationship to the fusion gain of a scenario and to the amount of current that can be driven by auxiliary sources [13, 18, 19]. These scenarios aim to operate at high values of the plasma $\beta$ (ratio of kinetic to magnetic pressure) to maximize the bootstrap current fraction. However, MHD instabilities, such as neoclassical tearing modes (NTMs), can be triggered in these regimes [20], which in turn limit the plasma performance and can lead to plasma-terminating disruptions. This complex set of interactions makes the problems of predicting and experimentally achieving high performance scenarios extremely challenging, and motivates the design of model-based feedback controllers to regulate plasma conditions.

Active control of the entire $q$ profile to drive the plasma magnetic profile to a suitable target may provide sufficiently stabilizing effects near rational $q$-surfaces to mitigate NTM formation and contribute to maximizing the bootstrap current [21]. To optimize the fusion power, the plasma density and temperature profiles must also simultaneously be controlled. The volume-averaged plasma stored energy is related to these kinetic plasma profiles and can alternatively be controlled to regulate the fusion power. The ability to robustly achieve and maintain particular plasma targets, in particular on long-pulse devices such as ITER where the resistive current diffusion time constant is comparable to the discharge time, through feedback can enable the study of desired regimes, control the proximity to stability limits and maximize the physics output of the executed plasma discharges.

### *1.1. Previous work*

Advances in magnetic profile control at the JET, DIII-D, Tore Supra and JT-60U tokamaks is described in [22–40] and simulation testing of profile control algorithms for ITER are described in [27, 41]. Recent experiments at DIII-D [28–31] represent the first successful demonstration of FPD, physics-model-based, closed-loop control of the entire magnetic profile evolution in a tokamak device. In the DIII-D experiments [28–31], the closed-loop control was chosen to be performed in low confinement (L-mode) scenarios because the coupling between the magnetic and kinetic plasma parameters is not as strong in this operating mode. As a result, the dynamics of the magnetic profile evolution in L-mode are simplified, which in turn reduced the complexity of the model-based control design process. Therefore, L-mode operating scenarios were more attractive for initial demonstration of the technical feasibility of controlling the magnetic profile evolution in closed-loop experiments with controllers synthesized from a FPD model. To extend this FPD control philosophy to high confinement (H-mode), high performance operating scenarios, the model employed to design the control algorithm needs to be extended to include the more complex physical phenomena in this operating regime. Progress towards physics-based, control-oriented modeling of the plasma evolution following a FPD approach has been recently reported [42–44].

### *1.2. Contributions of this work*

In this work, we first develop a general control-oriented physics-based modeling approach to obtain FPD models of the plasma magnetic profile and stored energy evolutions valid for H-mode, high performance plasma scenarios. High confinement operating scenarios in tokamaks are characterized by particle and energy transport barriers just inside the plasma boundary, which improve the plasma performance and result in the formation of large gradients in both the plasma density and temperature that increase the complexity of the coupling between the magnetic and kinetic plasma parameters via the increase of the plasma self-generated bootstrap current.

We begin the model development process by considering the well known one-dimensional poloidal magnetic flux diffusion equation [45, 46], which describes the poloidal magnetic flux profile evolution in the tokamak in response to the electric field due to induction and the noninductive current driven by the auxiliary heating and current-drive (H & CD) systems and the neoclassical bootstrap effect, in section 2. In section 3, simplified control-oriented versions of physics-based models of the electron density profile, the electron temperature profile, the plasma resistivity and the noninductive current-drives (auxiliary and bootstrap) valid for H-mode plasma scenarios are developed. The objective in developing these simplified physics-based models is to capture the dominant physics that describe how the control actuators affect the evolution of the plasma magnetic and kinetic profiles in H-mode scenarios. Additionally, in the development of the simplified models, we model the effects of the auxiliary heating/current-drive actuators independently, rather than lumping them into a single input as was done in [43], to exploit the full capabilities of a H & CD system. By combining the poloidal magnetic flux diffusion equation with these physics-based control-oriented models, a FPD, nonlinear, partial differential equation (PDE) model of the magnetic profile evolution valid for H-mode scenarios in the tokamak is developed in section 4. Finally, by employing a zero-dimensional, volume-averaged energy balance, a nonlinear ordinary differential equation (ODE) model of the plasma stored energy evolution in the tokamak is also obtained.

The FPD models of the plasma magnetic profile and stored energy dynamics are tailored to H-mode burning plasma scenarios in the ITER tokamak by employing the DINA-CH & CRONOS [5–9] free-boundary tokamak simulation code (also referred to as 'simulation code' hereafter) to obtain simulated

data of the plasma state evolution that is utilized to close the simplified physics-based models of the plasma parameters in section 5. This advanced simulation code couples the free-boundary plasma equilibrium and current diffusion solver DINA-CH [6] with the plasma heat and particle transport solver CRONOS [7] and employs complex physics models to predict the plasma magnetic and thermal state evolution in the tokamak through computationally intensive numerical simulations. The simulation code is currently configured to execute with a prescribed electron density evolution and calculates anomalous heat conductivity profiles using a global transport model, KIAUTO [47]. The radial heat conductivity profile dependence for the core plasma is computed using a gyroBohm-like formula. Additionally, the auxiliary heating/current-drive source profiles are recomputed by the simulation code on a one second time interval, and the plasma evolves with constant auxiliary powers in-between these auxiliary source profile updates. Finally, the FPD model's prediction capabilities are demonstrated by comparing the prediction to data obtained from DINA-CH & CRONOS simulations for ITER.

The developed FPD model is next used to design a physics-model-based algorithm to control the $q$ profile and stored energy evolutions in H-mode burning plasma scenarios in ITER. The control strategy employed is a feedforward + feedback control scheme in which the feedforward control commands are computed off-line and the feedback control commands are computed on-line. The objective of the feedforward controller is to achieve a target plasma state evolution throughout the discharge while taking into account actuator constraints, such as the maximum available amount of auxiliary heating/current-drive power and total plasma current ramp-up rate, and plasma state constraints, such as a $q$ profile with a minimum value higher or equal to one. To add robustness to the control strategy, the output of the feedforward controller is augmented with the output of a feedback controller. The objective of the feedback controller is to reject the effects of external disturbances to the plasma, overcome the uncertainties in the model used for the control design and regulate the plasma state around the target. In this work, physical quantities are used as actuators, although they are quantities which are themselves controlled by feedback loops. Thus, quantities such as the plasma current and plasma density are considered as actuators since they appear as control inputs in the developed FPD models. In other words, the proposed control algorithms will generate references for the respective physical quantities that are sent to the dedicated feedback control loops that command the physical actuators on the tokamak. Additionally, we exploit the fact that the dynamics of the physical actuator feedback control loops are faster than that of the system we are controlling, i.e. we assume that the dedicated control loops are able to instantaneously follow the references generated by the controllers developed in this work. As a result, the fact that the physical quantities have power supplies and gas valves is not taken into account here.

In the second part of this work, we focus on the design of the feedback portion of the overall control strategy (details on the design of the feedforward component of the control scheme following an optimization approach can be found in [48, 49]). In section 6, the feedback controller is designed (i) by embedding a FPD model of the plasma magnetic profile evolution into the control design process and (ii) to be *robust* to uncertainties in the electron density, electron temperature and plasma resistivity profiles, which are modeled as a nominal profile plus a bounded uncertain profile by defining ranges in which the plasma parameters are expected to be in typical ITER H-mode scenarios, i.e. to ensure the closed-loop system remains stable for an expected range of the plasma parameters. The feedback algorithm employs ITER's auxiliary heating/current-drive sources (three electron cyclotron (gyrotron) launchers, one ion cyclotron launcher, one total neutral beam injector) and the total plasma current as actuators to control the $q$ profile and stored energy evolution. In the scenarios considered in this work, the ion cyclotron launcher is configured to provide only heating power to the plasma. Therefore, we design the algorithm with a two loop structure. The first loop utilizes the total plasma current and exclusively the current-drive capabilities of the gyrotron and neutral beam launchers to control the $q$ profile, and the second loop utilizes the ion cyclotron launcher to control the stored energy. Other advances in developing FPD, physics-model-based algorithms to control the plasma dynamics can be found in [50–57]. In section 7 the feedback control algorithm is successfully tested in both reference tracking and disturbance rejection simulations with the developed FPD model of the plasma magnetic profile and stored energy evolution for ITER. We emphasize the scenarios studied in this work are not meant to be representative of any one specific standard ITER operating scenario but are meant to determine (i) the ability of the developed FPD model to predict the plasma magnetic and thermal state evolution in response to changes in the control actuators, and (ii) the ability of the designed feedback control algorithm to drive the plasma state evolution to a specified *physically achievable* target evolution. The effectiveness of the controller is demonstrated by first tracking nominal $q$ profile and stored energy target evolutions, and then modulating the generated fusion power while maintaining the $q$ profile in a stationary condition. Finally, a summary and discussion of some of the key practical issues investigated in this work for plasma profile control in ITER are presented in section 8.

## 2. First-principles modeling of the tokamak magnetic profile evolution

Any arbitrary quantity that is constant on each magnetic flux surface within the tokamak plasma can be used to index the magnetic flux surfaces. In this work, we choose the mean effective minor radius $\rho$ of the magnetic flux surface, i.e. $\Phi(\rho) = \pi B_{\phi,0}\rho^2$, as the indexing variable, where $\Phi$ is the toroidal magnetic flux and $B_{\phi,0}$ is the vacuum toroidal magnetic field at the geometric major radius $R_0$ of the tokamak. The normalized effective minor radius is defined as $\hat{\rho} = \rho/\rho_b$, where $\rho_b$ is the mean effective minor radius of the last closed magnetic flux surface. The evolution of the poloidal magnetic

flux is given in normalized cylindrical coordinates by the magnetic diffusion equation [45, 46]

$$\frac{\partial\psi}{\partial t} = \frac{\eta(T_e)}{\mu_0\rho_b^2\hat{F}^2}\frac{1}{\hat{\rho}}\frac{\partial}{\partial\hat{\rho}}\left(\hat{\rho}\hat{F}\hat{G}\hat{H}\frac{\partial\psi}{\partial\hat{\rho}}\right) + R_0\hat{H}\eta(T_e)\frac{\langle\bar{j}_{ni}\cdot\bar{B}\rangle}{B_{\phi,0}}, \quad (1)$$

where $\psi$ is the poloidal stream function, which is closely related to the poloidal flux $\Psi$, i.e. $\Psi = 2\pi\psi$, $t$ is the time, $\eta$ is the plasma resistivity, $T_e$ is the electron temperature, $\mu_0$ is the vacuum magnetic permeability, $\bar{j}_{ni}$ is any source of noninductive current density (electron cyclotron heating/current-drive, neutral beam heating/current-drive, bootstrap current-drive, etc), $\bar{B}$ is the magnetic field and $\langle\rangle$ denotes a flux-surface average. The parameters $\hat{F}$, $\hat{G}$ and $\hat{H}$ are geometric factors pertaining to the magnetic configuration of a particular plasma equilibrium (see [2, 43] for instance), which are functions of $\hat{\rho}$, and are defined as,

$$\hat{F}(\hat{\rho}) = \frac{R_0B_{\phi,0}}{RB_\phi} \qquad \hat{G}(\hat{\rho}) = \left\langle\frac{R_0^2}{R^2}|\nabla\rho|^2\right\rangle,$$
$$\hat{H}(\hat{\rho}) = \frac{\hat{F}}{\langle R_0^2/R^2\rangle},$$

where $R$ denotes the radial spatial coordinate in the poloidal plane of the tokamak and $B_\phi$ is the toroidal magnetic field. The boundary conditions are given by

$$\left.\frac{\partial\psi}{\partial\hat{\rho}}\right|_{\hat{\rho}=0} = 0 \qquad \left.\frac{\partial\psi}{\partial\hat{\rho}}\right|_{\hat{\rho}=1} = -\frac{\mu_0}{2\pi}\frac{R_0}{\hat{G}(1)\hat{H}(1)}I_{\mathrm{p}}(t), \quad (2)$$

where $I_{\mathrm{p}}(t)$ is the total plasma current. The model (1) and (2) makes the simplifying assumption that the magnetic geometry is fixed in time [43], which excludes two potential sources of flux: (i) a change in $\rho_b$, either by a change in the shape of the last closed flux surface or in $B_{\phi,0}$ and (ii) a change in location of the geometric center of the interior flux surfaces relative to that of the last closed flux surface, such as changes in the Shafranov shift that occur during a plasma $\beta$ or internal inductance change. The assumption that the plasma shape can be considered fixed assumes that a separate poloidal field (PF) coil controller, which is not considered here, regulates the last closed flux surface.

## 3. Control-oriented physics-based modeling of plasma parameters

The objective in developing the control-oriented physics-based models of the electron density profile, the electron temperature profile, the plasma resistivity and the noninductive current-drives is to capture the dominant physics that describe how the control actuators affect the plasma parameters and hence the magnetic profile evolution. We emphasize that the models developed are not designed for physical understanding, rather they are meant to capture the dominant physics which affect the overall system dynamics that are relevant for control design, i.e. the input–output relationship of the system. This implies that a controller synthesized by employing the control-oriented model only needs to know about the physics that are relevant to its design objective, which is to control the magnetic profile evolution. The simplified models are developed with particular care being taken to ensure their applicability to H-mode scenarios.

### 3.1. Actuators for magnetic profile control in tokamaks

There are several actuators that can be used to manipulate the plasma magnetic profile evolution in the tokamak. The first actuator is the total plasma current, which is controlled by the PF coil system. By controlling the total current inside the last closed magnetic flux surface, the internal magnetic profile can be modified through resistive diffusion. Also, since the plasma is slightly resistive, some of the plasma current is dissipated into heat. The plasma resistivity scales inversely with the plasma electron temperature ($\propto T_e^{-3/2}$), therefore, at high temperatures the resistive diffusion is low, which tends to freeze the magnetic profile evolution. The second actuator is neutral beam injection (NBI). Injecting beams of highly energetic neutral particles into the plasma provides a source of noninductive current as well as plasma heating through collisions. The third actuator is radio-frequency heating/current-drive. On ITER, the frequency can be tuned to excite the electrons or ions by power from electron cyclotron and ion cyclotron launchers, respectively, and the radio frequency waves can be injected into the plasma in a variety of ways to achieve various combinations of electron/ion cyclotron resonant heating (ECRH/ICRH) and electron/ion cyclotron current drive (ECCD/ICCD). The final actuator is the plasma electron density, which is controlled by gas-feed and pellet launchers. However, tight control of the electron density in experiments is challenging due to large recycling at the walls.

### 3.2. Electron density modeling

In the formulation of the electron density model, we assume that the control action employed to regulate the electron density only weakly affects the radial distribution of the electrons. Therefore, the electron density evolution $n_e(\hat{\rho},t)$ is modeled as

$$n_e(\hat{\rho},t) = n_e^{\mathrm{prof}}(\hat{\rho})\bar{n}_e(t), \quad (3)$$

where $n_e^{\mathrm{prof}}(\hat{\rho})$ is a reference electron density profile and $\bar{n}_e(t)$ is the line average electron density, which is typically utilized to specify the electron density in present tokamak operation. Note that $n_e^{\mathrm{prof}}$ is obtained by evaluating the experimental/simulated $n_e$ at a reference time $t_{r_{n_e}}$, i.e. $n_e^{\mathrm{prof}}(\hat{\rho}) = n_e(\hat{\rho},t_{r_{n_e}})/\bar{n}_e(t_{r_{n_e}})$.

### 3.3. Electron temperature modeling

In the formulation of the model of the electron temperature evolution, we assume a tight coupling between the electron and ion species in the plasma, i.e. $T_e(\hat{\rho},t)\approx T_i(\hat{\rho},t)$ and $n_e(\hat{\rho},t)\approx n_i(\hat{\rho},t)$, where $T_i(\hat{\rho},t)$ and $n_i(\hat{\rho},t)$ are the ion

temperature and density profiles, respectively. As a result, we neglect the explicit electron–ion equilibration power in the development of the model and also fuel dilution by impurities, although impurities return into the control-oriented model via Bremsstrahlung radiation and plasma resistivity. Under these assumptions, the plasma kinetic pressure $p$ and stored energy density $W_d$ are expressed as

$$\begin{aligned} p(\hat{\rho},t) &= n_e(\hat{\rho},t)T_e(\hat{\rho},t) + n_i(\hat{\rho},t)T_i(\hat{\rho},t) \\ &= 2n_e(\hat{\rho},t)T_e(\hat{\rho},t), \\ W_d(\hat{\rho},t) &= \frac{3}{2}n_e(\hat{\rho},t)T_e(\hat{\rho},t) + \frac{3}{2}n_i(\hat{\rho},t)T_i(\hat{\rho},t) \\ &= 3n_e(\hat{\rho},t)T_e(\hat{\rho},t). \end{aligned} \tag{4}$$

To model the electron temperature profile evolution, we employ an approximate singular perturbation approach that exploits the fact that the characteristic thermal diffusion time in the plasma is much faster than the characteristic resistive diffusion time. Therefore the temperature is always in quasi-equilibrium on the time-scale of the current evolution, and we neglect the temporal dynamics of the electron temperature in the development of the electron temperature evolution model as we are mainly concerned with capturing the dominant physical effects that the electron temperature has on the plasma magnetic profile evolution.

As a result of the edge energy transport barrier that develops in H-mode plasmas, the plasma temperature may exhibit a different behavior in the plasma core (inside of the transport barrier) and near the plasma boundary (outside of the transport barrier) in this regime. The slowly evolving (on the resistive current diffusion time scale) electron temperature profile evolution $T_e(\hat{\rho},t)$ is modeled as a static map of the control actuators as

$$\begin{aligned} T_e(\hat{\rho},t) = {} & k_{T_e,1}(\hat{\rho})[T_e^{\text{prof}}(\hat{\rho}) - T_e^{\text{prof}}(\hat{\rho}_{tb})]I_p(t)^{\gamma}P_{\text{tot}}(t)^{\varepsilon}n_e(\hat{\rho},t)^{\zeta} \\ & + k_{T_e,2}(\hat{\rho}_{tb})^{\omega}T_e^{\text{prof}}(\hat{\rho}_{tb})I_p(t)^{\lambda}P_{\text{tot}}(t)^{\nu}n_e(\hat{\rho}_{tb},t)^{\xi} \end{aligned} \tag{5}$$

in the plasma core ($0 \leqslant \hat{\rho} < \hat{\rho}_{tb}$) and as

$$T_e(\hat{\rho},t) = k_{T_e,2}(\hat{\rho})^{\omega}T_e^{\text{prof}}(\hat{\rho})I_p(t)^{\lambda}P_{\text{tot}}(t)^{\nu}n_e(\hat{\rho},t)^{\xi} \tag{6}$$

outside of the plasma edge energy transport barrier ($\hat{\rho}_{tb} \leqslant \hat{\rho} \leqslant 1$), where $k_{T_e,1}(\hat{\rho})$ and $k_{T_e,2}(\hat{\rho})$ are spatial constants, $T_e^{\text{prof}}(\hat{\rho})$ is a reference electron temperature profile, $P_{\text{tot}}(t)$ is the total power injected into the plasma and $\hat{\rho}_{tb}$ is the spatial location of the edge energy transport barrier in the plasma. To arrive at the scaling shown in (5) and (6), first a steady-state, zero-dimensional plasma energy balance is considered, i.e. $W/\tau_W \approx 3\langle n_e\rangle_V\langle T_e\rangle_V V_p/\tau_W = P_{\text{tot}}$, where $W$ is the total plasma stored energy, $\tau_W$ is the energy confinement time, $\langle\cdot\rangle_V$ denotes the volume-average operation $1/V_p\int_V(\cdot)\mathrm{d}V$, $V$ is the volume enclosed by a magnetic flux surface and $V_p$ is the total plasma volume (assuming $T_e = T_i$ and $n_e = n_i$). Many energy confinement scaling laws have been developed over the years, and typically these scaling laws are functions of the actuators used for plasma control, i.e. $\tau_W \propto I_p^{\gamma_s}P_{\text{tot}}^{\varepsilon_s}\langle n_e\rangle_V^{\zeta_s}$, where $\gamma_s$, $\varepsilon_s$ and $\zeta_s$ depend on the particular scaling law used. The scaling in the electron temperature model shown in (5) is inspired by the form of $T_e$ when the steady-state zero-dimensional energy balance equation is solved assuming the above scaling law, i.e. $\langle T_e\rangle_V \propto I_p^{\gamma}P_{\text{tot}}^{\varepsilon}\langle n_e\rangle_V^{\zeta}$ with $\gamma = \gamma_s$, $\varepsilon = 1 + \varepsilon_s$ and $\zeta = \zeta_s - 1$. The same principle applies for the scaling outside of the plasma edge energy transport barrier in (6). Modeling the electron temperature evolution in this manner provides the ability to incorporate the potential different plasma response inside of and outside of the edge energy transport barrier. The constants $\gamma$, $\varepsilon$ and $\zeta$ describe how the temperature in the plasma core scales with the various parameters, and the constants $\lambda$, $\nu$ and $\xi$ describe how the temperature outside of the plasma edge transport barrier scales with the various parameters. The constant $\omega$ is 1 if the temperature outside of the edge energy transport barrier scales with the various plasma parameters, i.e. $\lambda$, $\nu$, $\xi$ are not all equal to 0, and the constant $\omega$ is 0 if the temperature outside of the edge energy transport barrier does not scale with the plasma parameters, i.e. $\lambda$, $\nu$, $\xi$ are all equal to 0. Note that $T_e^{\text{prof}}$ is obtained by evaluating the experimental/simulated $T_e$ at a reference time $t_{r_{T_e}}$, i.e. $T_e^{\text{prof}}(\hat{\rho}) = T_e(\hat{\rho}, t_{r_{T_e}})$. The constants $k_{T_e,1}$ and $k_{T_e,2}$ are also evaluated at a reference time $t_{r_{T_e}}$ and are expressed as

$$\begin{aligned} k_{T_e,1}(\hat{\rho}) &= [I_p(t_{r_{T_e}})^{\gamma}P_{\text{tot}}(t_{r_{T_e}})^{\varepsilon}n_e(\hat{\rho},t_{r_{T_e}})^{\zeta}]^{-1}, \\ k_{T_e,2}(\hat{\rho}) &= [I_p(t_{r_{T_e}})^{\lambda}P_{\text{tot}}(t_{r_{T_e}})^{\nu}n_e(\hat{\rho},t_{r_{T_e}})^{\xi}]^{-1}, \end{aligned}$$

where $k_{T_e,1}$ is defined on the interval $0 \leqslant \hat{\rho} < \hat{\rho}_{tb}$ and $k_{T_e,2}$ is defined on the interval $\hat{\rho}_{tb} \leqslant \hat{\rho} \leqslant 1$.

The total power injected into the plasma $P_{\text{tot}}(t)$ is expressed as

$$P_{\text{tot}}(t) = P_{\text{ohm}}(t) + P_{\text{aux}}(t) - P_{\text{rad}}(t) + \eta_{\text{fus}}P_{\text{fus}}(t), \tag{7}$$

where $P_{\text{ohm}}(t)$ is the ohmic power, $P_{\text{aux}}(t)$ is the total auxiliary H & CD power, $P_{\text{rad}}(t)$ is the radiated power, $P_{\text{fus}}(t)$ is the fusion power and the effectiveness of the fusion power in heating the plasma is captured through the efficiency constant $\eta_{\text{fus}}$. The ohmic power is expressed as

$$P_{\text{ohm}}(t) = \int_0^1 j_{\text{tor}}^2(\hat{\rho},t)\eta(\hat{\rho},t)\frac{\mathrm{d}V}{\mathrm{d}\hat{\rho}}\mathrm{d}\hat{\rho} \approx \mathcal{R}_p(t)I_p(t)^2, \tag{8}$$

where $j_{\text{tor}}(\hat{\rho},t)$ is the toroidal current density and $\mathcal{R}_p$ is the global plasma resistance, which is expressed as

$$\mathcal{R}_p(t) \approx \frac{2\pi R_0}{\int_0^1\left[\frac{1}{\eta(\hat{\rho},t)}\frac{\mathrm{d}S}{\mathrm{d}\hat{\rho}}\mathrm{d}\hat{\rho}\right]},$$

where $S$ is the poloidal cross-sectional area enclosed by a magnetic flux surface within the plasma. The total auxiliary heating/current-drive power is expressed as

$$\begin{aligned} P_{\text{aux}}(t) = {} & \sum_{i=1}^{n_{\text{ec}}}\eta_{\text{ec}_i}P_{\text{ec}_i}(t) + \sum_{i=1}^{n_{\text{ic}}}\eta_{\text{ic}_i}P_{\text{ic}_i}(t) \\ & + \sum_{i=1}^{n_{\text{nbi}}}\eta_{\text{nbi}_i}P_{\text{nbi}_i}(t), \end{aligned} \tag{9}$$

where $P_{\text{ec}_i}(t)$ is the power in the individual gyrotron launchers, $P_{\text{ic}_i}(t)$ is the power in the individual ion cyclotron launchers, $P_{\text{nbi}_i}(t)$ is the power in the individual neutral beam injectors, and $n_{\text{ec}}$, $n_{\text{ic}}$ and $n_{\text{nbi}}$ are the total number of gyrotron,

ion cyclotron and neutral beam launchers, respectively. The effectiveness each respective heating source has on increasing the total stored energy in the plasma is captured through the efficiency constants $\eta_{\mathrm{ec}_i}$, $\eta_{\mathrm{ic}_i}$ and $\eta_{\mathrm{nbi}_i}$, respectively.

The radiative power density losses are modeled as

$$Q_{\mathrm{rad}} = k_{\mathrm{brem}} Z_{\mathrm{eff}} n_e(\hat{\rho},t)^2 \sqrt{T_e(\hat{\rho},t)}, \tag{10}$$

where $k_{\mathrm{brem}} = 5.5 \times 10^{-37}\,\mathrm{Wm}^3/\sqrt{\mathrm{keV}}$ is the Bremsstrahlung radiation coefficient and $Z_{\mathrm{eff}}$ is the effective atomic number of the ions in the plasma, which is defined as

$$Z_{\mathrm{eff}} = \frac{1}{n_e} \sum_{\text{all ions}} n_j Z_j^2, \tag{11}$$

where $n_j$ and $Z_j$ are the density and atomic number of the $j$th ion species. In this work, we assume $Z_{\mathrm{eff}}$ to be constant in space and time, however, a spatial dependence could straightforwardly be incorporated in this approach. The radiated power is then expressed as

$$P_{\mathrm{rad}}(t) = \int_0^1 Q_{\mathrm{rad}}(\hat{\rho},t) \frac{\mathrm{d}V}{\mathrm{d}\hat{\rho}} \mathrm{d}\hat{\rho}. \tag{12}$$

The power denstity provided by fusion reactions is expressed as

$$Q_{\mathrm{fus}}(\hat{\rho},t) = Q_{\mathrm{DT}} n_{\mathrm{D}}(\hat{\rho},t) n_{\mathrm{T}}(\hat{\rho},t) \langle\sigma v\rangle_{\mathrm{DT}}(\hat{\rho},t) k_{\mathrm{JeV}}, \tag{13}$$

where $Q_{\mathrm{DT}} = 17.6$ MeV is the energy released in each D–T reaction, $n_{\mathrm{D}}(\hat{\rho},t)$ and $n_{\mathrm{T}}(\hat{\rho},t)$ are the density of the deuterium and tritium ions, respectively, and $k_{\mathrm{JeV}} = e \times 1\,\mathrm{V\,eV}^{-1}$, where $e$ is the elementary charge in units of Coulombs. Note that by neglecting the alpha particle and impurity densities, the charge neutrality condition in the plasma can be approximated as $n_e(\hat{\rho},t) \approx n_{\mathrm{D}}(\hat{\rho},t) + n_{\mathrm{T}}(\hat{\rho},t) \approx 2n_{\mathrm{DT}}(\hat{\rho},t)$, where a 50 : 50 mix of deuterium and tritium ions is assumed and $n_{\mathrm{DT}}$ is the deuterium–tritium density. Under these assumptions, the fusion power density (13) can be approximated as

$$Q_{\mathrm{fus}}(\hat{\rho},t) \approx Q_{\mathrm{DT}} \left(\frac{n_e(\hat{\rho},t)}{2}\right)^2 \langle\sigma v\rangle_{\mathrm{DT}}(\hat{\rho},t) k_{\mathrm{JeV}}. \tag{14}$$

The deuterium–tritium reactivity $\langle\sigma v\rangle_{\mathrm{DT}}$ is dependent on the velocity distribution of the deuterium and tritium ions, which is a nonlinear function of the deuterium and tritium temperature $T_{\mathrm{DT}}(\hat{\rho},t)$. From [58], $\langle\sigma v\rangle_{\mathrm{DT}}$ is given in units of $\mathrm{cm}^3{\cdot}\mathrm{s}^{-1}$by

$$\langle\sigma v\rangle_{\mathrm{DT}}(\hat{\rho},t) = \exp\left(\frac{a_1}{T_{\mathrm{DT}}^r} + a_2 + a_3 T_{\mathrm{DT}} + a_4 T_{\mathrm{DT}}^2 + a_5 T_{\mathrm{DT}}^3 + a_6 T_{\mathrm{DT}}^4\right), \tag{15}$$

where $T_{\mathrm{DT}}$ is in keV, the constants $a_i$ and $r$ are given in table 1 of [58] and we have neglected non-thermal ions which might enhance the reactivity. Under our working assumption of an approximately equal electron and ion temperature we evaluate (15) with $T_{\mathrm{DT}} = T_e(\hat{\rho},t)$. The fusion power is then expressed as

$$P_{\mathrm{fus}}(t) = \int_0^1 Q_{\mathrm{fus}}(\hat{\rho},t) \frac{\mathrm{d}V}{\mathrm{d}\hat{\rho}} \mathrm{d}\hat{\rho}. \tag{16}$$

### 3.4. Plasma resistivity modeling

Following a simplified Spitzer resistivity model, the plasma resistivity $\eta(T_e)$ scales with the electron temperature as

$$\eta(\hat{\rho},t) = \frac{k_{sp}(\hat{\rho}) Z_{\mathrm{eff}}}{T_e(\hat{\rho},t)^{3/2}}, \tag{17}$$

where $k_{sp}$ is a constant, which is expressed as

$$k_{sp}(\hat{\rho}) = \frac{\eta(\hat{\rho},t_{r_\eta}) T_e(\hat{\rho},t_{r_\eta})^{3/2}}{Z_{\mathrm{eff}}}.$$

Note that $k_{sp}$ is evaluated at a reference time $t_{r_\eta}$. We neglect neoclassical corrections to this formula, which can nonetheless be significant, to retain the main dependence.

### 3.5. Noninductive current-drive modeling

The total noninductive current-drive is produced by the gyrotron launchers, the neutral beam injection and the bootstrap current and is expressed as

$$\frac{\langle \bar{j}_{ni} \cdot \bar{B}\rangle}{B_{\phi,0}} = \sum_{i=1}^{n_{\mathrm{ec}}} \frac{\langle \bar{j}_{\mathrm{ec}_i} \cdot \bar{B}\rangle}{B_{\phi,0}} + \sum_{i=1}^{n_{\mathrm{nbi}}} \frac{\langle \bar{j}_{\mathrm{nbi}_i} \cdot \bar{B}\rangle}{B_{\phi,0}} + \frac{\langle \bar{j}_{\mathrm{bs}} \cdot \bar{B}\rangle}{B_{\phi,0}}, \tag{18}$$

where $\bar{j}_{\mathrm{ec}_i}$ is the noninductive current generated by the individual gyrotron launchers, $\bar{j}_{\mathrm{nbi}_i}$ is the noninductive current generated by the individual neutral beam injectors and $\bar{j}_{\mathrm{bs}}$ is the noninductive current generated by the bootstrap effect. In the operating scenarios considered in this work, the ion cyclotron launchers are configured to provide only heating power to the plasma.

#### 3.5.1. Electron cyclotron and neutral beam injection current-drive.

We model each auxiliary noninductive current-source as the time varying power in each actuator multiplied by a constant deposition profile in space. The current density provided by each auxiliary source is modeled as

$$\frac{\langle \bar{j}_i \cdot \bar{B}\rangle}{B_{\phi,0}}(\hat{\rho},t) = k_i(\hat{\rho}) j_i^{\mathrm{dep}}(\hat{\rho}) \frac{T_e(\hat{\rho},t)^\delta}{n_e(\hat{\rho},t)} \eta_i P_i(t) = j_i^{\mathrm{ref}}(\hat{\rho}) \frac{T_e(\hat{\rho},t)^\delta}{n_e(\hat{\rho},t)} \eta_i P_i(t), \tag{19}$$

where $i \in [\mathrm{ec}_1, \ldots, \mathrm{ec}_{n_{\mathrm{ec}}}, \mathrm{nbi}_1, \ldots, \mathrm{nbi}_{n_{\mathrm{nbi}}}]$, $k_i$ is a constant, $j_i^{\mathrm{dep}}(\hat{\rho})$ is a reference deposition profile for each current-drive source, the term $T_e^\delta/n_e$ represents the current-drive/absorption efficiency and $j_i^{\mathrm{ref}} = k_i j_i^{\mathrm{dep}}$. For electron cyclotron current-drive, $\delta = 1$ [19] and for neutral beam current-drive, $\delta$ is dependent on the energy of the injected particles [18]. Note that $j_i^{\mathrm{dep}}$ is evaluated at a reference time $t_{r_{\mathrm{aux}}}$, i.e. $j_i^{\mathrm{dep}}(\hat{\rho}) = [\langle \bar{j}_i \cdot \bar{B}\rangle / B_{\phi,0}](\hat{\rho}, t_{r_{\mathrm{aux}}})$. The constants $k_i$ are expressed as

$$k_i(\hat{\rho}) = \frac{n_e(\hat{\rho}, t_{r_{\mathrm{aux}}})}{T_e(\hat{\rho}, t_{r_{\mathrm{aux}}})^\delta \eta_i P_i(t_{r_{\mathrm{aux}}})}.$$

Note that the constants $k_i$ are also evaluated at the time $t_{r_{\text{aux}}}$.

*3.5.2. Bootstrap current-drive.* The bootstrap current [12] is associated with trapped particles and arises from the inhomogeneity of the magnetic field strength produced by the external coils in the tokamak, which falls off like $1/R$. From [59, 60], we write the bootstrap current as

$$\frac{\langle \vec{j}_{\text{bs}} \cdot \vec{B} \rangle}{B_{\phi,0}} = \frac{RB_\phi(\psi)}{B_{\phi,0}} p_e \left[ \mathcal{L}_{31} \left\{ \frac{1}{p_e}\frac{\partial p_e}{\partial \psi} + \frac{1}{p_e}\frac{\partial p_i}{\partial \psi} \right\} + \mathcal{L}_{32}\frac{1}{T_e}\frac{\partial T_e}{\partial \psi} + \mathcal{L}_{34}\alpha \frac{1-R_{pe}}{R_{pe}}\frac{1}{T_i}\frac{\partial T_i}{\partial \psi} \right], \quad (20)$$

where $p_e$ denotes the electron pressure, $p_i$ denotes the ion pressure and $R_{pe} = p_e/p$ where $p$ is the total plasma pressure. Note the opposite sign of (20) due to the different definition of $\psi$. Under our working assumption of a tight coupling between the electron and ion species in the plasma, i.e. $T_e \approx T_i$ and $n_e \approx n_i$, we can write $p_e = n_e T_e = n_i T_i = p_i$ and $R_{pe} = (n_e T_e)/(n_e T_e + n_i T_i) = 1/2$. Substituting these relationships into (20) we obtain

$$\frac{\langle \vec{j}_{\text{bs}} \cdot \vec{B} \rangle}{B_{\phi,0}}(\hat{\rho},t) = \frac{k_{\text{JkeV}} R_0}{\hat{F}(\hat{\rho})} \left( \frac{\partial \psi}{\partial \hat{\rho}} \right)^{-1} \left[ 2\mathcal{L}_{31}(\hat{\rho}) T_e(\hat{\rho},t) \frac{\partial n_e}{\partial \hat{\rho}} + \{ 2\mathcal{L}_{31}(\hat{\rho}) + \mathcal{L}_{32}(\hat{\rho}) + \alpha(\hat{\rho})\mathcal{L}_{34}(\hat{\rho}) \} n_e(\hat{\rho},t) \frac{\partial T_e}{\partial \hat{\rho}} \right], \quad (21)$$

where the coefficients $\mathcal{L}_{31}(\hat{\rho})$, $\mathcal{L}_{32}(\hat{\rho})$, $\mathcal{L}_{34}(\hat{\rho})$ and $\alpha(\hat{\rho})$ depend on the magnetic configuration of a particular plasma equilibrium and on particle collisionality in the plasma and $k_{\text{JkeV}} = 1000 \times k_{\text{JeV}}$.

## 4. First-principles-driven model of plasma poloidal magnetic flux profile and stored energy evolutions

### 4.1. Poloidal magnetic flux profile response model

By combining the simplified versions of physics-based models of the electron density profile (3), electron temperature profile (5) and (6), plasma resistivity (17) and noninductive current-drives (18), (19) and (21) introduced in section 3 with the magnetic diffusion equation model (1) and (2) presented in section 2, we obtain our desired FPD control-oriented model of the poloidal magnetic flux profile evolution. At this time, we stress that we have included the dominant physics properties of the tokamak plasma that are critical to the evolution of the poloidal magnetic flux profile in response to the various actuators (from a control point-of-view), and have neglected others. An example of this is illustrated by including $Z_{\text{eff}}$ for plasma resistivity (17) and Bremsstrahlung radiation (10), but not for fuel dilution. Our purpose is to include the dominant features, which will ultimately be verified by modeling as well as the performance of control algorithms designed by employing the developed FPD model.

By defining the control input vector as

$$u = [P_{\text{ec}_1}, \ldots, P_{\text{ec}_{n_{\text{ec}}}}, P_{\text{ic}_1}, \ldots, P_{\text{ic}_{n_{\text{ic}}}}, P_{\text{nbi}_1}, \ldots, P_{\text{nbi}_{n_{\text{nbi}}}}, \bar{n}_e, I_{\text{p}}],$$

the FPD, nonlinear, PDE model is expressed as

$$\frac{\partial \psi}{\partial t} = f_\eta(\hat{\rho}, u(t)) \frac{1}{\hat{\rho}} \frac{\partial}{\partial \hat{\rho}} \left( \hat{\rho} D_\psi \frac{\partial \psi}{\partial \hat{\rho}} \right) + \sum_{i=1}^{n_{\text{ec}}} f_{\text{ec}_i}(\hat{\rho}, u(t)) P_{\text{ec}_i}(t) + \sum_{i=1}^{n_{\text{nbi}}} f_{\text{nbi}_i}(\hat{\rho}, u(t)) P_{\text{nbi}_i}(t) + f_{\text{bs}}(\hat{\rho}, u(t)) \left( \frac{\partial \psi}{\partial \hat{\rho}} \right)^{-1}, \quad (22)$$

with boundary conditions

$$\left. \frac{\partial \psi}{\partial \hat{\rho}} \right|_{\hat{\rho}=0} = 0 \qquad \left. \frac{\partial \psi}{\partial \hat{\rho}} \right|_{\hat{\rho}=1} = -k_{I_{\text{p}}} I_{\text{p}}(t), \quad (23)$$

where the parameters $f_\eta$, $f_{\text{ec}_i}$, $f_{\text{nbi}_i}$ and $f_{\text{bs}}$ are functions of the model parameters, the diffusion coefficient $D_\psi$ is defined as $D_\psi(\hat{\rho}) = \hat{F}(\hat{\rho})\hat{G}(\hat{\rho})\hat{H}(\hat{\rho})$ and $k_{I_{\text{p}}} = [\mu_0 R_0]/[2\pi \hat{G}(1)\hat{H}(1)]$. In the case where the electron temperature in the plasma core and outside of the edge energy transport barrier scales in an identical way with the plasma parameters, i.e. $\gamma = \lambda$, $\varepsilon = \nu$, $\zeta = \xi$ and $\omega = 1$, the spatial and temporal dependence in the model parameters $f_\eta$, $f_{\text{ec}_i}$, $f_{\text{nbi}_i}$ and $f_{\text{bs}}$ can be separated and (22) can be expressed as

$$\frac{\partial \psi}{\partial t} = f_\eta(\hat{\rho}) u_\eta(t) \frac{1}{\hat{\rho}} \frac{\partial}{\partial \hat{\rho}} \left( \hat{\rho} D_\psi \frac{\partial \psi}{\partial \hat{\rho}} \right) + \sum_{i=1}^{n_{\text{ec}}} f_{\text{ec}_i}(\hat{\rho}) u_{\text{ec}_i}(t) + \sum_{i=1}^{n_{\text{nbi}}} f_{\text{nbi}_i}(\hat{\rho}) u_{\text{nbi}_i}(t) + f_{\text{bs}}(\hat{\rho}) u_{\text{bs}}(t) \left( \frac{\partial \psi}{\partial \hat{\rho}} \right)^{-1}, \quad (24)$$

where the control inputs are written as

$$\begin{aligned} u_\eta(t) &= [I_{\text{p}}(t)^\gamma P_{\text{tot}}(t)^\varepsilon \bar{n}_e(t)^\zeta]^{-3/2}, \\ u_{\text{ec}_i}(t) &= [I_{\text{p}}(t)^\gamma P_{\text{tot}}(t)^\varepsilon \bar{n}_e(t)^\zeta]^{-1/2} \bar{n}_e(t)^{-1} P_{\text{ec}_i}(t), \\ u_{\text{nbi}_i}(t) &= [I_{\text{p}}(t)^\gamma P_{\text{tot}}(t)^\varepsilon \bar{n}_e(t)^\zeta]^{(-3/2+\delta)} \bar{n}_e(t)^{-1} P_{\text{nbi}_i}(t), \\ u_{\text{bs}}(t) &= [I_{\text{p}}(t)^\gamma P_{\text{tot}}(t)^\varepsilon \bar{n}_e(t)^\zeta]^{-1/2} \bar{n}_e(t). \end{aligned} \quad (25)$$

From (24), we see that the magnetic diffusion equation admits actuation not only through interior control ($u_{\text{ec}_i}, u_{\text{nbi}_i}, u_{\text{bs}}$) and boundary control ($I_{\text{p}}$), but also through $u_\eta$, which we name *diffusivity control* in this work. Simulated/experimental data can now be utilized to identify the various reference profiles and model constants in the simplified physics-based models (3), (5), (6), (17)–(19) and (21) to tailor the FPD, control-oriented model (22) and (23) to an operating scenario of interest in a particular device. As the device and scenario change, the dependence of the parameters $f_\eta$, $f_{\text{ec}_i}$, $f_{\text{nbi}_i}$ and $f_{\text{bs}}$ on $\hat{\rho}$ will change, but the structure of (22) and (23) will remain the same and control algorithms for various devices can be designed based on one model structure.

### *4.2. Model augmentation by zero-dimensional stored energy response model*

Under the assumption of a tight coupling between the electron and ion species in the plasma, the stored energy in the plasma is expressed as

$$\begin{aligned} W &= k_{\mathrm{JkeV}}\Bigg[\int_0^1\left(\frac{3}{2}n_e(\hat{\rho},t)T_e(\hat{\rho},t)\right.\\ &\quad\left.+\frac{3}{2}n_i(\hat{\rho},t)T_i(\hat{\rho},t)\right)\frac{\mathrm{d}V}{\mathrm{d}\hat{\rho}}\mathrm{d}\hat{\rho}\Bigg],\\ &= k_{\mathrm{JkeV}}\int_0^1 W_d\frac{\mathrm{d}V}{\mathrm{d}\hat{\rho}}\mathrm{d}\hat{\rho}. \end{aligned} \tag{26}$$

For control design purposes, it is desirable to obtain a dynamic mapping describing the evolution of the stored energy in the plasma in response to the control actuators. In this work, we employ a zero-dimensional, volume-averaged, approximate plasma energy balance equation. Assuming the plasma volume does not change in time, the approximate energy balance equation is given by the nonlinear ODE

$$\begin{aligned} \frac{\mathrm{d}\bar{W}}{\mathrm{d}t} &= -P_{\mathrm{loss}}+P_{\mathrm{ohm}}+P_{\mathrm{aux}}-P_{\mathrm{rad}}+\eta_{\mathrm{fus}}P_{\mathrm{fus}},\\ &= -\frac{\bar{W}}{\tau_{\bar{W}}}+P_{\mathrm{ohm}}+\sum_{i=1}^{n_{\mathrm{ec}}}\eta_{\mathrm{ec}_i}P_{\mathrm{ec}_i}+\sum_{i=1}^{n_{\mathrm{ic}}}\eta_{\mathrm{ic}_i}P_{\mathrm{ic}_i}\\ &\quad+\sum_{i=1}^{n_{\mathrm{nbi}}}\eta_{\mathrm{nbi}_i}P_{\mathrm{nbi}_i}-P_{\mathrm{rad}}+\eta_{\mathrm{fus}}P_{\mathrm{fus}}, \end{aligned} \tag{27}$$

where $\bar{W}$ is the approximate stored energy, $P_{\mathrm{loss}}=\bar{W}/\tau_{\bar{W}}$ is the total power crossing the separatrix and $\tau_{\bar{W}}$ is the global energy confinement time. The energy confinement scaling used in this work is the IPB98($y$,2) scaling law [61]

$$\begin{aligned} \tau_{\bar{W}} &= 0.0562H_{H98(y,2)}I_{\mathrm{p}}(\mathrm{MA})^{0.93}R_0(\mathrm{m})^{1.39}a(\mathrm{m})^{0.58}\\ &\quad\bar{n}_e(10^{19}\mathrm{m}^{-3})^{0.41}B_{\phi,0}(\mathrm{T})^{0.15}A_{\mathrm{eff}}^{0.19}\\ &\quad\kappa^{0.78}P_{\mathrm{tot}}(\mathrm{MW})^{-0.69}, \end{aligned} \tag{28}$$

where $H_{H98(y,2)}$ is the energy confinement enhancement factor, $a$ is the plasma minor radius, $A_{\mathrm{eff}}$ is the effective mass number of the hydrogenic ion species in the plasma and $\kappa$ is the plasma elongation.

### *4.3. Relevant output plasma parameters*

There are many parameters related to the plasma magnetic and thermal states, $\psi$ and $\bar{W}$, respectively, that will be of interest in determining the type of operating scenarios that are or can be achieved and their performance. The parameters considered in this work are the $q$ profile, the toroidal current density ($j_{\mathrm{tor}}$), the normalized plasma beta ($\beta_{\mathrm{N}}$) and the plasma loop voltage profile ($U_{\mathrm{p}}$). The safety factor profile is related to the spatial gradient of the poloidal magnetic flux profile and is defined as

$$q(\hat{\rho},t)=-\frac{\mathrm{d}\Phi}{\mathrm{d}\Psi}=-\frac{\mathrm{d}\Phi}{2\pi\mathrm{d}\psi}=-\frac{B_{\phi,0}\rho_b^2\hat{\rho}}{\partial\psi/\partial\hat{\rho}}, \tag{29}$$

where we have utilized the definitions of the mean effective minor radius of the magnetic flux surfaces $\Phi(\rho)=\pi B_{\phi,0}\rho^2$ and the normalized mean effective minor radius $\hat{\rho}=\rho/\rho_b$. The toroidal current density is also related to the poloidal magnetic flux spatial gradient and is defined as [4]

$$j_{\mathrm{tor}}(\hat{\rho},t)=-\frac{1}{\mu_0\rho_b^2R_0\hat{H}}\frac{1}{\hat{\rho}}\frac{\partial}{\partial\hat{\rho}}\left(\hat{\rho}\hat{G}\hat{H}\frac{\partial\psi}{\partial\hat{\rho}}\right). \tag{30}$$

The normalized plasma beta is related to the plasma stored energy and is defined as

$$\beta_{\mathrm{N}}=\beta_t[\%]\frac{aB_{\phi,0}}{I_{\mathrm{p}}[\mathrm{MA}]}\qquad \beta_t=\frac{\langle p\rangle_V}{B_{\phi,0}^2/(2\mu_0)}=\frac{(2/3)(\bar{W}/V_{\mathrm{p}})}{B_{\phi,0}^2/(2\mu_0)}, \tag{31}$$

where $\beta_t$ is the toroidal plasma beta, we have assumed a tight coupling between the electron and ion species in the plasma and we have utilized (4) and (26). The plasma loop voltage profile is related to the temporal derivative of the poloidal magnetic flux profile and is defined as

$$U_{\mathrm{p}}(\hat{\rho},t)=-\frac{\partial\Psi}{\partial t}=-2\pi\frac{\partial\psi}{\partial t}. \tag{32}$$

### *4.4. Model-order reduction for simulation*

In order to reduce the dimensionality of the FPD model, we spatially discretize the infinite dimensional PDE (22) and (23) by employing a finite difference method, where the non-dimensional spatial domain of interest ($\hat{\rho}\in[0,1]$) is represented by $m$ discrete nodes. After spatially discretizing (22) and taking into account the boundary conditions (23), we obtain a nonlinear finite dimensional ODE model defined by

$$\dot{\hat{\psi}}=f_{\psi}(\hat{\psi},u),$$

where $\hat{\psi}=[\psi_2,\psi_3,\ldots,\psi_{m-1}]^T\in\mathbb{R}^n$ is the plasma magnetic state vector, $\psi_i$ is the value of $\psi$ at the discrete nodes, $f_{\psi}\in\mathbb{R}^n$ is a nonlinear function of the plasma magnetic states and control inputs and $n=m-2$. By defining the augmented plasma state vector as

$$x=\begin{bmatrix}\hat{\psi}\\ \bar{W}\end{bmatrix}\in\mathbb{R}^{n+1},$$

we can write the magnetic and kinetic system dynamics as

$$\dot{x}=\begin{bmatrix}f_{\psi}(\hat{\psi},u)\\ -\dfrac{\bar{W}}{\tau_{\bar{W}}}+P_{\mathrm{tot}}\end{bmatrix}=F_{\psi,\bar{W}}(x,u)\in\mathbb{R}^{n+1}. \tag{33}$$

## 5. Tailoring first-principles-driven model to the ITER tokamak

We now employ the DINA-CH & CRONOS free-boundary simulation code [5–9] configured to the ITER geometry to

obtain simulated data of the plasma state evolution to tailor the FPD model to H-mode burning plasma scenarios in ITER that have energy and particle transport barriers just inside the plasma boundary. In section 5.1, the model parameters tailored to the ITER tokamak are presented and in section 5.2 a simulation study that compares the evolution of the plasma parameters predicted by the FPD model and the simulation code is discussed.

### *5.1. Model tailored to the ITER tokamak*

Following Goldston's scaling law [62], the scaling parameters in (5) are chosen as $\gamma = 1$, $\varepsilon = 0.5$ and $\zeta = -1$. This choice qualitatively describes the electron temperature evolution in the core of the plasma in response to the control actuators, i.e. the observation of (i) an increase in plasma confinement, and hence an increase in temperature, with increasing plasma current, and (ii) a decrease in plasma confinement with increasing total injected power [62]. Also, by changing the electron density, the electron temperature is modified by the proposed model for a given electron pressure. Based on the electron temperature profile evolution predicted by the simulation code, the scaling parameters in (6) are chosen as $\omega = 0 \Rightarrow \lambda = \nu = \xi = 0$, which models the temperature outside of the edge energy transport barrier as stiff. The auxiliary H & CD actuators used are 3 independently configurable gyrotron launchers, 1 ion cyclotron launcher and co-current-injection neutral beam launchers. In the considered operating scenarios, (i) the ion cyclotron launcher is configured to provide only heating power to the plasma and (ii) the neutral beam launchers are configured to inject particles at the same off-axis radial location, therefore, we group them together to form 1 total neutral beam launcher. The energy of the injected neutral particles on ITER is 1 MeV, therefore, the constant in the neutral beam current-drive model (19) is chosen as $\delta = 1$ [18].

The parameters related to the magnetic configuration of the plasma equilibrium, the reference profiles for the various models and the normalizing profiles are shown in figure 1. In this work, the heating efficiency constants for the auxiliary heating/current-drive actuators are taken as the ratio between the power absorbed by the plasma (calculated by the simulation code) and the power requested for each individual actuator, and the efficiency constants are $\eta_{\mathrm{ec}_i} = 1$ for $i = 1, 2, 3$, $\eta_{\mathrm{ic}} = 0.85$ and $\eta_{\mathrm{nbi}} = 1$. We choose the heating efficiency constant related to alpha particle heating in (7) as $\eta_{\mathrm{fus}} = 0.15$ so that the plasma stored energy predicted by the simplified physics-based model (26) matches the plasma stored energy predicted by the simulation code. Employing these heating efficiency constants, the energy confinement enhancement factor is chosen as $H_{H98(y,\,2)} = 1.3$ [8], so that the volume-averaged, approximate energy balance equation (27) predicts the same energy confinement enhancement, and hence plasma stored energy, as the simulation code. Finally, the other model constants are $B_{\phi,0} = 5.3\,\mathrm{T}$, $R_0 = 6.2$ m, $a = 2.0$ m, $\rho_b = 2.62$ m, $\hat{\rho}_{tb} = 0.95$, $\kappa = 1.7$, $Z_{\mathrm{eff}} = 1.7$ and $A_{\mathrm{eff}} = 2.5$.

### *5.2. Comparison between first-principles-driven model and DINA-CH & CRONOS predictions*

We now describe a simulation study that compares the evolution of the plasma parameters predicted by the FPD model and the DINA-CH & CRONOS free-boundary simulation code [5–9]. We emphasize that the scenario studied is not meant to be representative of any one specific standard ITER operating scenario but is meant to determine the ability of the FPD model to predict the plasma magnetic and thermal state evolution in response to changes in the control actuators. As the FPD model is designed for the high performance phase of the discharge, we start the simulations just after the plasma transitions from L-mode to H-mode in this particular simulated scenario at the time $t = 45$ s, which is still in the plasma current ramp-up phase. The control inputs (total plasma current, individual gyrotron launcher, ion cyclotron launcher and neutral beam injection powers and line average electron density) applied during both simulations are shown in figure 2(a). We begin the analysis of the FPD model's prediction capabilities by first comparing the prediction of the simplified physics-based models of the electron density profile, the electron temperature profile and the noninductive current-drive source evolutions to the evolutions of these plasma parameters predicted by the simulation code. Figures 2(e) and (f) show the electron density profile, figures 2(b)–(d) show the electron and ion temperature profiles and figure 3 shows the total gyrotron, neutral beam injection and bootstrap noninductive current-drive sources at various times during the simulations computed by both the simplified physics-based models and the simulation code.

The trends of the plasma parameters predicted by the simplified physics-based models show good agreement with those predicted by the simulation code. Firstly, as shown in figures 2(b) and (d), the simulation code predicts that the electron and ion temperature profiles evolve in a similar fashion, which suggests that the simplified physics-based model assumption of an approximately equal electron and ion temperature appears appropriate for the scenarios considered. Secondly, as shown in figures 3(b) and (d), the simulation code predicts that the spatial noninductive current deposition location of the gyrotron launchers and neutral beam injectors remains reasonably constant throughout the simulation. Therefore, the simplified physics-based model assumption of constant gyrotron and neutral beam injection current deposition profiles also appears appropriate for the scenarios considered. Finally, as shown in figures 3(c) and (d), the simplified physics-based model prediction of the noninductive current driven by the neutral beam injectors agrees reasonably well with the neutral beam driven noninductive current predicted by the simulation code. However, the simplified physics-based model neglects the slowing down time of the fast ions, assuming that the particles and their energy are instantaneously thermalized, but this physical mechanism is taken into account by the simulation code. This effect can be seen at the time $t = 50$ s during the simulations. A first-order filter could straightforwardly be included in the simplified model to describe this physical mechanism.

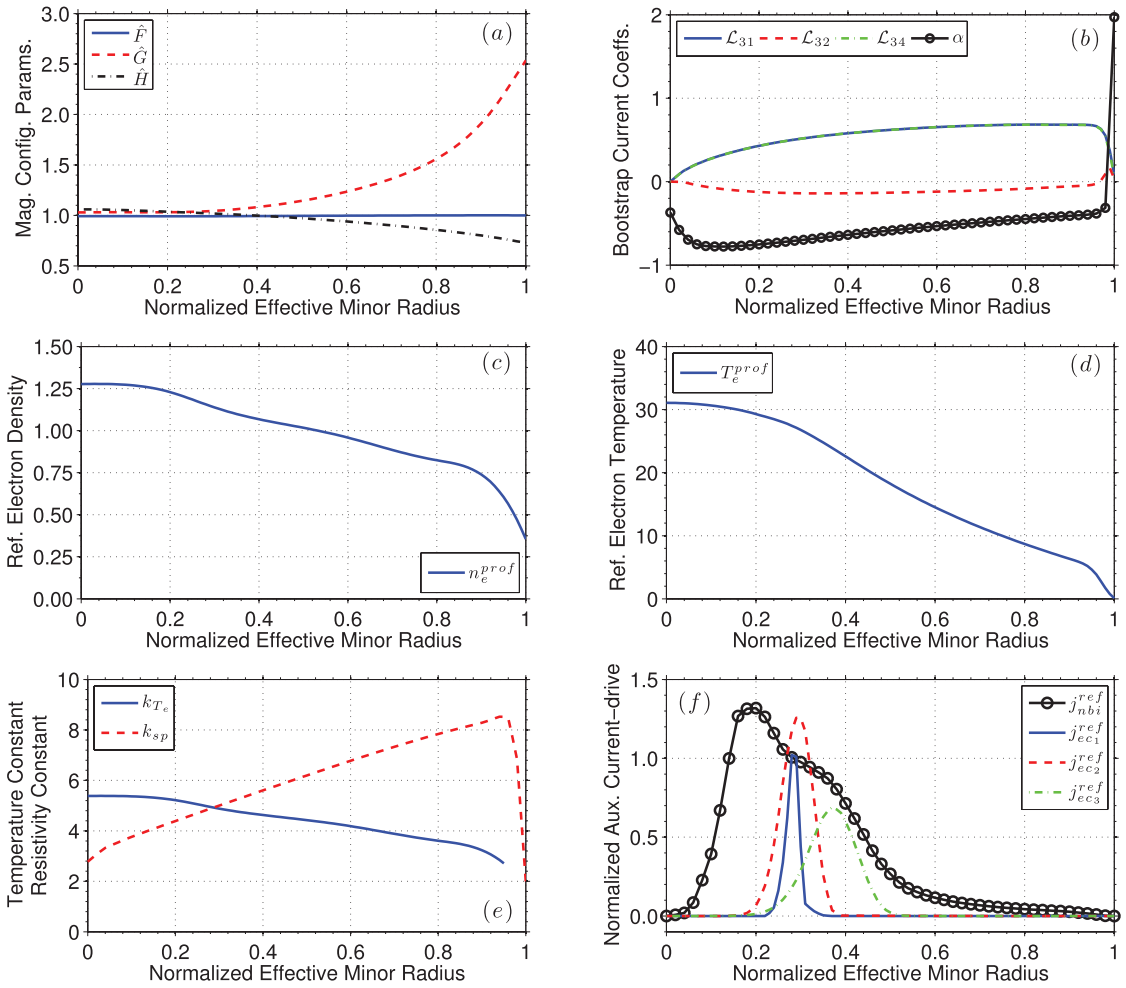


**Figure 1.** Model parameters tailored to the ITER tokamak: (a) magnetic equilibrium configuration parameters $\hat{F}(\hat{\rho})$, $\hat{G}(\hat{\rho})$ and $\hat{H}(\hat{\rho})$, (b) bootstrap current coefficients $\mathcal{L}_{31}(\hat{\rho})$, $\mathcal{L}_{32}(\hat{\rho})$, $\mathcal{L}_{34}(\hat{\rho})$ and $\alpha(\hat{\rho})$ (computed from definitions in [59, 60]), (c) reference electron density profile $n_e^{\text{prof}}(\hat{\rho})$, (d) reference electron temperature profile $T_e^{\text{prof}}(\hat{\rho})$ (keV), (e) electron temperature coefficient $k_{T_e} = k_{T_e,1}$ ($10^8$ m$^{-3}$ A$^{-1}$ W$^{-1/2}$), note $k_{T_e,2} = 1$, and plasma resistivity coefficient $k_{sp}$ ($10^{-8}$ Ω m keV$^{3/2}$), (e) normalized auxiliary neutral beam injection ($j_{\text{nbi}}^{\text{ref}}$) and electron cyclotron ($j_{\text{ec}_1}^{\text{ref}}$, $j_{\text{ec}_2}^{\text{ref}}$, $j_{\text{ec}_3}^{\text{ref}}$) current-drive reference profiles ($10^{17}$ m$^{-3}$ keV$^{-1}$ W$^{-1}$ A m$^{-2}$).

We now compare the plasma magnetic and thermal state evolution, as well as several related plasma parameters, predicted by the FPD control-oriented model and the simulation code. Figure 4 shows the evolution of the poloidal magnetic flux Ψ at various normalized effective minor radii, figures 5–7 show a comparison of the FPD-model-predicted and simulation-code-predicted safety factor $q(\hat{\rho})$, toroidal current density $j_{\text{tor}}(\hat{\rho})$ and loop voltage $U_{\text{p}}(\hat{\rho})$ profiles, respectively, at various times and figure 8 shows a comparison of the FPD-model-predicted and simulation-code-predicted plasma stored energy $\bar{W}$, normalized plasma beta $\beta_{\text{N}}$ and fusion power $P_{\text{fus}}$.

The scenario studied can be broken into four time sections: (i) 45–85 s, (ii) 85–200 s, (iii) 200–250 s and (iv) 250–400 s, as shown in figure 2(a). During section (i) of the simulation, the control inputs are modified in time from their initial values to a first set of constant values and during section (ii) of the simulation, the control inputs remain stationary. During section (iii) of the simulation, the control inputs are again modified to a second set of constant values and again remain stationary during section (iv) of the simulation. This sequence of actuator waveforms provides the opportunity to determine the ability of the FPD model to predict the plasma magnetic and thermal state evolution during both transient and stationary conditions in plasma actuation. Figures 4–8 show that the trends (plasma response directions to changes in the control actuators) of the FPD-model-predicted plasma magnetic and thermal state evolution, as well as the other parameters related to these plasma states, show good agreement with the simulation-code-predicted results during both transient and stationary plasma actuation conditions. The mismatch in the safety factor profile (figure 5) and the current density profile (figure 6) for $\hat{\rho} \leqslant 0.2$ is a result of the neutral beam current density deviation when large step changes in the neutral beam power are introduced. This deviation is due to neglecting the slowing down time of the neutral particles in the control model as discussed above. This deviation in current density then affects the time evolution of the $q$ profile in the plasma core. The discontinuity in the plasma stored energy, normalized beta and fusion power predicted by the simulation code at 300 s, shown in figure 8, is a numerical artifact in the plasma

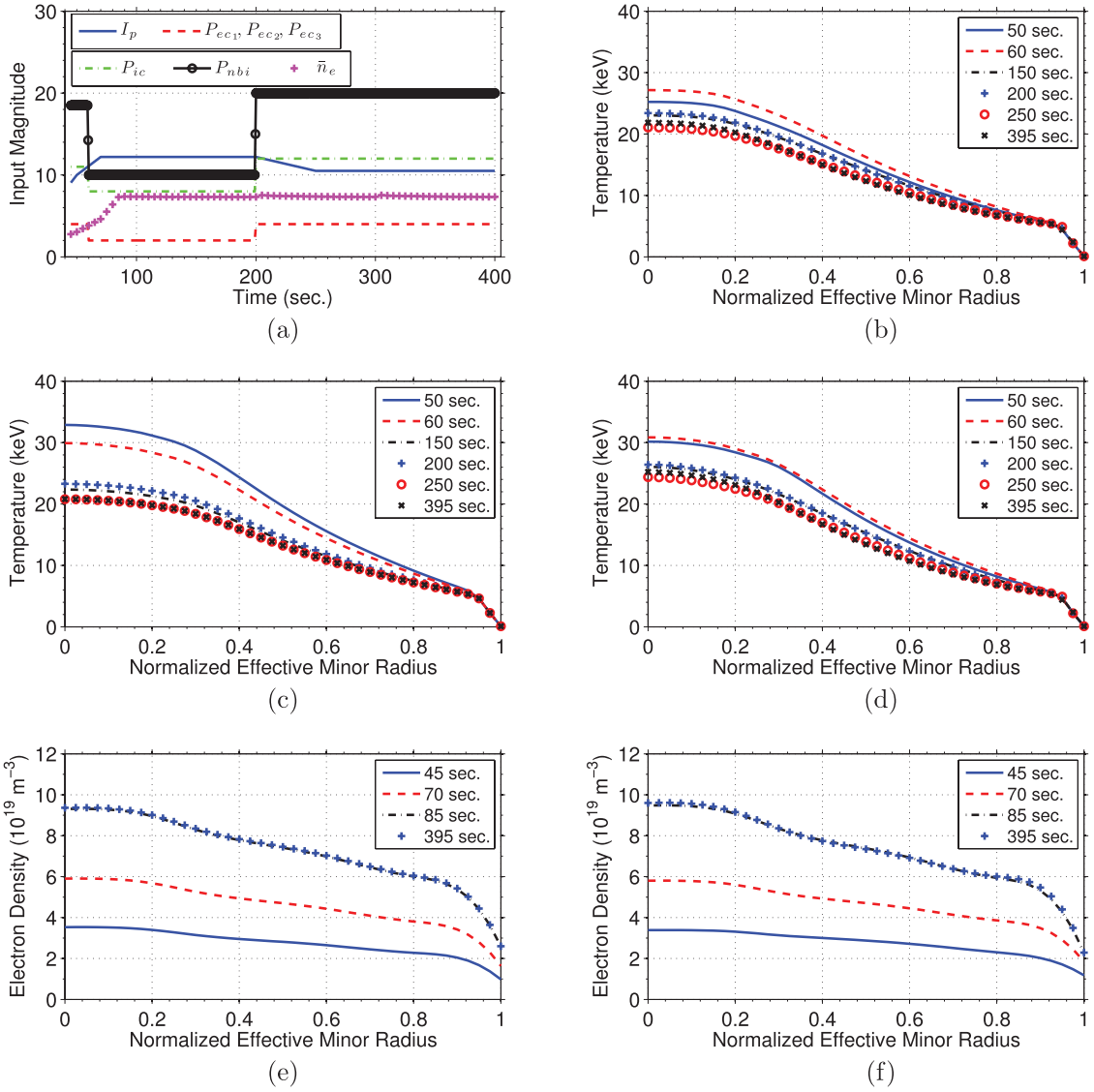


**Figure 2.** (a) Control inputs applied during the simulations based on the FPD model and the simulation code (current in MA, power in MW and density in $10^{19}$ m$^{-3}$). Ion temperature evolution computed via the simulation code shown in (b). Electron temperature profile evolution computed: (c) via the FPD control-oriented model and (d) via the simulation code. Electron density profile evolution computed: (e) via the FPD control-oriented model and (f) via the simulation code. In (e) and (f), the line for 85 s is nearly identical to the line for 395 s indicating that the electron density evolution reaches a stationary condition at 85 s This is in agreement with the line average electron density evolution shown in (a).

evolution that results from a slight inconsistency between the plasma state in a simulation that is restarted from a previously executed simulation.

## 6. Robust feedback control algorithm design

In this section, a model-based feedback control algorithm is designed to track target $q$ profile and stored energy evolutions in H-mode burning plasma scenarios in ITER by embedding a FPD model of the plasma magnetic profile evolution into the control design process. In the operating scenario considered in this work, the ion cyclotron launcher is configured to provide only heating power to the plasma. Therefore, we design the combined algorithm with a two loop structure. The first loop exclusively employs the current-drive capabilities of the total plasma current and the gyrotron and neutral beam launchers to control the $q$ profile, and the second loop utilizes the ion cyclotron launcher to control the plasma stored energy. This approach does not take into account the physical effects that the actuators have on the $q$ profile dynamics through plasma heating, which specifically affects the $q$ profile evolution through resistive diffusion, auxiliary current-drive efficiency and bootstrap current drive. Therefore, we first employ the developed FPD model of the plasma magnetic profile and stored energy evolution to study the effect that this control direction (pure plasma heating) has on the $q$ profile dynamics in the considered H-mode ITER scenarios in section 6.1. In section 6.2, we introduce the FPD model of the plasma magnetic profile state evolution that we employ to synthesize the $q$ profile portion of the feedback control algorithm. The feedback controller is designed to be *robust* to uncertainties

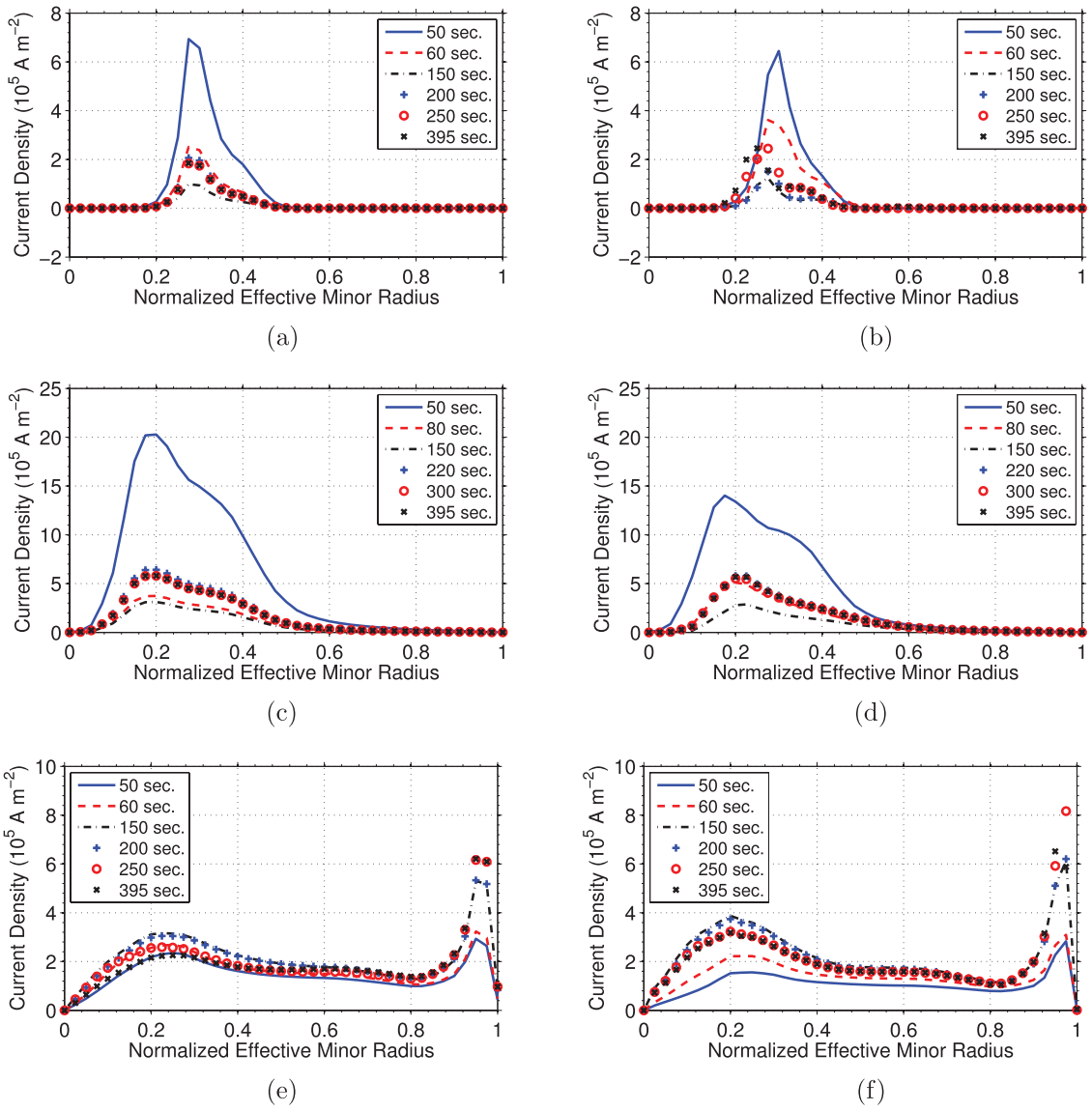


**Figure 3.** Noninductive current-drive evolution computed via the FPD control-oriented model: (a) total gyrotron, (c) neutral beam injection and (e) bootstrap and noninductive current-drive evolution computed via the simulation code: (b) total gyrotron, (d) neutral beam injection and (f) bootstrap.

in the electron density (not used as a control input), electron temperature and plasma resistivity profiles, i.e. to ensure the closed-loop system remains stable for an expected range of the plasma parameters, by following what is referred to as a *robust control design* approach [63] in the control theory literature in section 6.3. The interested reader is directed to appendix A, where a mathematical derivation of the $q$ profile feedback controller is provided.

### *6.1. Pure plasma heating effect on the safety factor profile*

We investigate the effect that pure plasma heating has on the $q$ profile in the considered H-mode ITER scenarios by using the FPD model described in sections 4 and 5 by allowing the plasma to evolve to a stationary state with physical actuator quantities of $I_{\mathrm{p}} = 11$ MA, $P_{\mathrm{ec}_1} = P_{\mathrm{ec}_2} = P_{\mathrm{ec}_3} = 4$ MW, $P_{\mathrm{nbi}} = 20$ MW and $\bar{n}_e = 7.35 \times 10^{19}$ m$^{-3}$ under low ion cyclotron heating conditions ($P_{\mathrm{ic}} = 5$ MW) and high ion cyclotron heating conditions ($P_{\mathrm{ic}} = 20$ MW). Note that the power injected through the ion cyclotron launcher in ITER is constrained to the range $0\ \mathrm{MW} \leqslant P_{\mathrm{ic}} \leqslant 20$ MW. A comparison of the auxiliary, bootstrap and toroidal current density for the low ($P_{\mathrm{ic}} = 5$ MW) and high ($P_{\mathrm{ic}} = 20$ MW) heating cases is shown in figures 9(a)–(c). The effect of increasing the electron temperature through plasma heating increases both the auxiliary and bootstrap current-drives as expected from (19) and (21). The increases in both off-axis auxiliary co-current-drive and off-axis bootstrap co-current-drive results in the toroidal current density decreasing in the spatial region $\hat{\rho} \in [0\,, 0.2)$ and slightly increasing in the spatial region $\hat{\rho} \in [0.2, 0.4]$. Note that as the total plasma current remains constant, the increase in off-axis current density requires a corresponding decrease in on-axis current density. The effect that this shift in equilibrium toroidal current density has on the $q$ profile is shown in figure 9(d), which shows that pure plasma heating in the considered H-mode scenarios in ITER

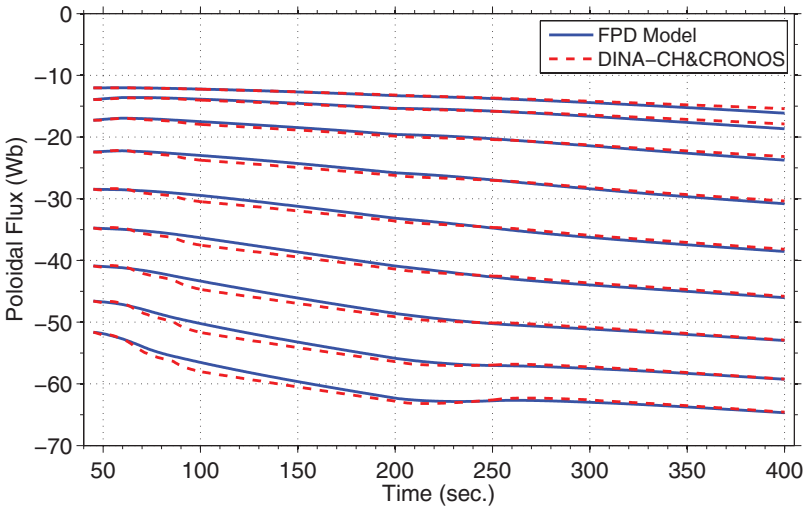


**Figure 4.** Time trace of poloidal magnetic flux $\Psi$ at various normalized effective minor radii (top to bottom $\hat{\rho} = 0.1, 0.2, \ldots, 0.8, 0.9$).

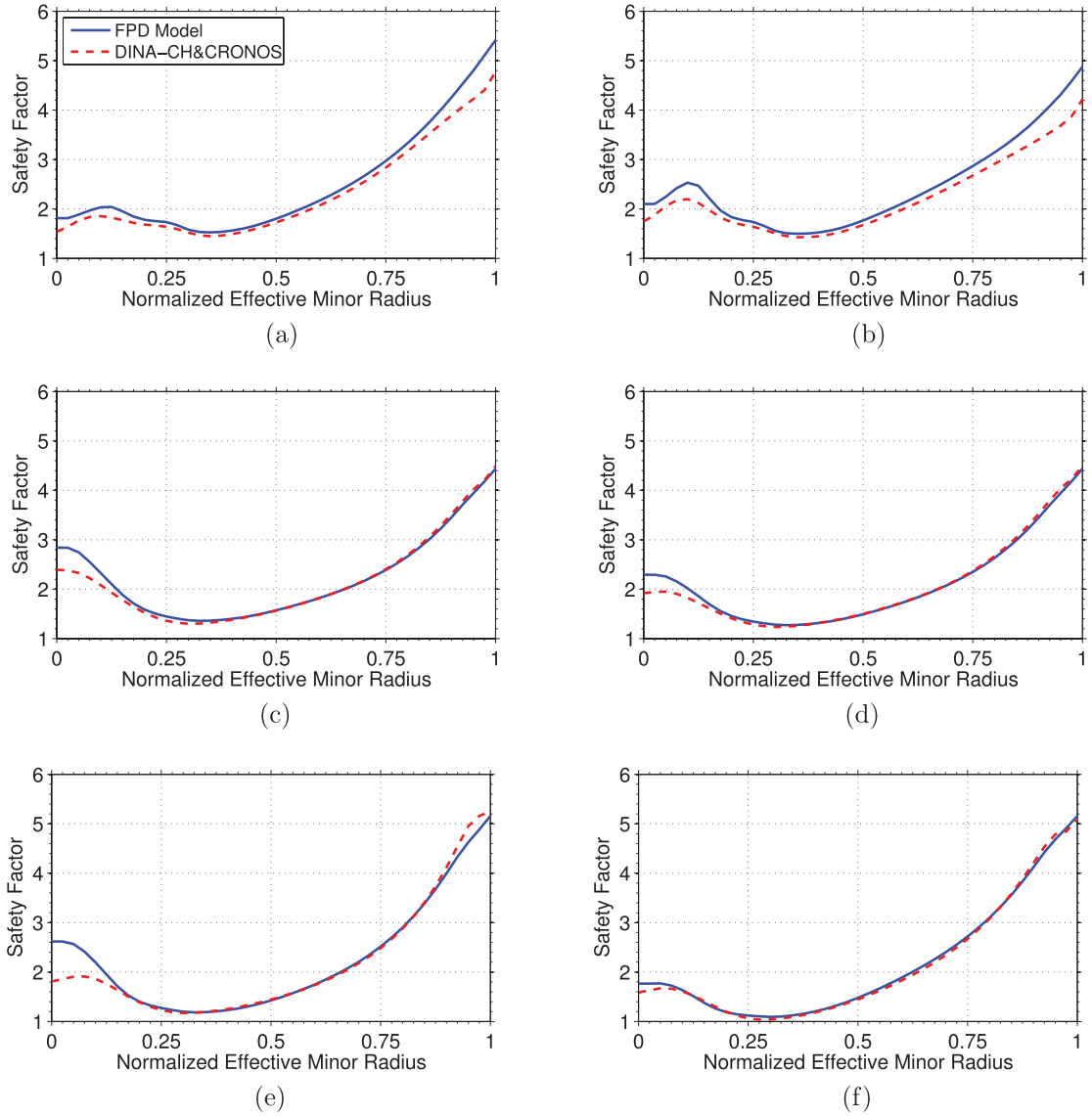


**Figure 5.** Safety factor profile $q(\hat{\rho})$ at various times. (a) $t = 50$ s. (b) $t = 60$ s. (c) $t = 150$ s. (d) $t = 200$ s. (e) $t = 250$ s. (f) $t = 395$ s.

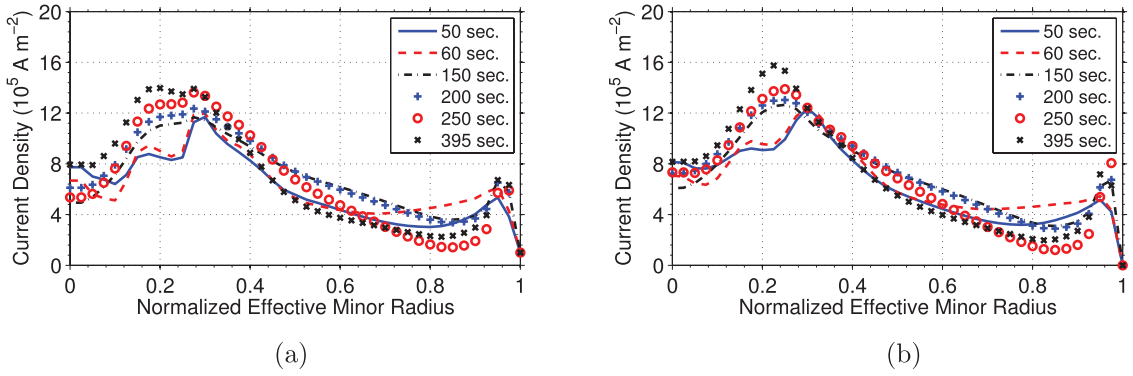


**Figure 6.** Toroidal current density evolution computed via: (a) FPD control-oriented model and (b) simulation code.

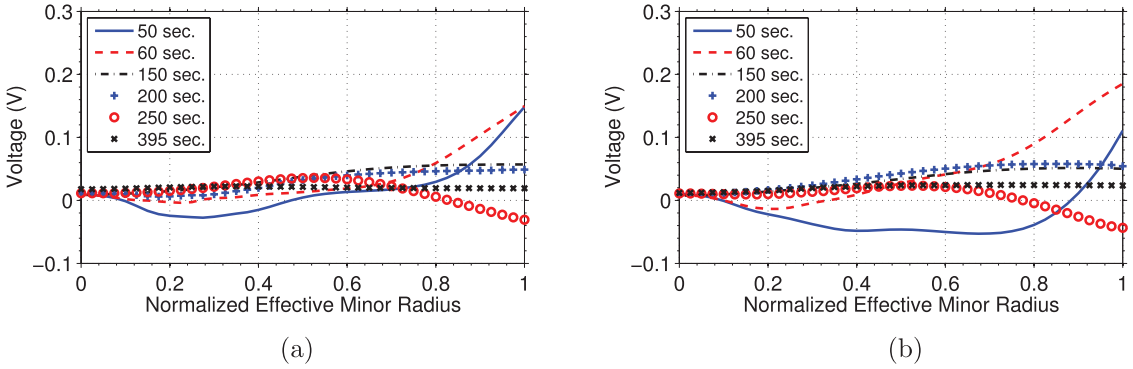


**Figure 7.** Loop voltage profile evolution computed via: (a) FPD control-oriented model and (b) simulation code.

results in approximately a 5% increase in the $q$ profile in the spatial region $\hat{\rho} \in [0\ ,\ 0.2)$ with a negligible change outside of this spatial region. Therefore, the actuators used for $q$ profile control will attempt to counteract any $q$ profile disturbance that results from plasma heating effects.

### *6.2. First-principles-driven model of plasma magnetic state evolution*

We begin by defining ranges in which the electron density and electron temperature profiles are expected to be in typical ITER high performance scenarios, which are shown in figures 10(a) and (b). For feedback control design, we model these kinetic plasma parameters as a nominal profile plus a bounded uncertain profile, i.e.

$$n_e(\hat{\rho}) = n_e^{\text{nom}}(\hat{\rho}) + n_e^{\text{unc}}(\hat{\rho})\delta_{n_e}, \tag{34}$$

$$T_e(\hat{\rho}) = T_e^{\text{nom}}(\hat{\rho}) + T_e^{\text{unc}}(\hat{\rho})\delta_{T_e}, \tag{35}$$

where $n_e^{\text{nom}}(\hat{\rho}) = [n_e^{\max}(\hat{\rho}) + n_e^{\min}(\hat{\rho})]/2$, $T_e^{\text{nom}}(\hat{\rho}) = [T_e^{\max}(\hat{\rho}) + T_e^{\min}(\hat{\rho})]/2$, $n_e^{\text{unc}}(\hat{\rho}) = [n_e^{\max}(\hat{\rho}) - n_e^{\min}(\hat{\rho})]/2$, and $T_e^{\text{unc}}(\hat{\rho}) = [T_e^{\max}(\hat{\rho}) - T_e^{\min}(\hat{\rho})]/2$. The superindex 'unc' has been used to denote the profiles associated with the uncertain parameters $\delta_{T_e}$ and $\delta_{n_e}$, which satisfy $|\delta_{T_e}| \leqslant 1$ and $|\delta_{n_e}| \leqslant 1$. The plasma resistivity decreases as the electron temperature increases, therefore, the minimum plasma resistivity is defined by the maximum electron temperature, and the maximum plasma resistivity is defined by the minimum electron temperature, and the resistivity range is shown in figure 10(c). Additionally, the parameter $1/n_e$ is related to the electron density. For feedback control design, these kinetic plasma parameters are modeled as

$$\eta(\hat{\rho}) = \eta^{\text{nom}}(\hat{\rho}) + \eta^{\text{unc}}(\hat{\rho})\delta_{T_e}, \tag{36}$$

$$1/n_e(\hat{\rho}) = n_e^{\text{nom}'}(\hat{\rho}) + n_e^{\text{unc}'}(\hat{\rho})\delta_{n_e}, \tag{37}$$

where $\eta^{\text{nom}}(\hat{\rho}) = [\eta^{\max}(\hat{\rho}) + \eta^{\min}(\hat{\rho})]/2$, $n_e^{\text{nom}'}(\hat{\rho}) = [n_e^{\max}(\hat{\rho}) + n_e^{\min}(\hat{\rho})]/[2n_e^{\max}(\hat{\rho})n_e^{\min}(\hat{\rho})]$, $\eta^{\text{unc}}(\hat{\rho}) = [\eta^{\min}(\hat{\rho}) - \eta^{\max}(\hat{\rho})]/2$, $n_e^{\text{unc}'}(\hat{\rho}) = [n_e^{\min}(\hat{\rho}) - n_e^{\max}(\hat{\rho})]/[2n_e^{\max}(\hat{\rho})n_e^{\min}(\hat{\rho})]$ and the plasma resistivity dependence on the electron temperature is modeled to first order to simplify the control design process.

From (29), we see that the safety factor profile is inversely related to the spatial gradient of the poloidal magnetic flux. Therefore, if we are able to control the poloidal flux gradient profile, which we define as

$$\theta(\hat{\rho}, t) \equiv \partial\psi/\partial\hat{\rho}(\hat{\rho}, t), \tag{38}$$

we will be able to control the $q$ profile, assuming the system is indeed controllable. By combining the poloidal magnetic flux diffusion equation (1) with the models (34) through (37) and the models of the noninductive current-drive sources (18), (19) and (21), we obtain an uncertain PDE model of the $\psi$ dynamics that is used for feedback control design. Expanding this equation by using the chain rule, inserting (38) into the expanded equation and differentiating the resulting equation with respect to $\hat{\rho}$, the PDE governing the evolution of $\theta$ is expressed as

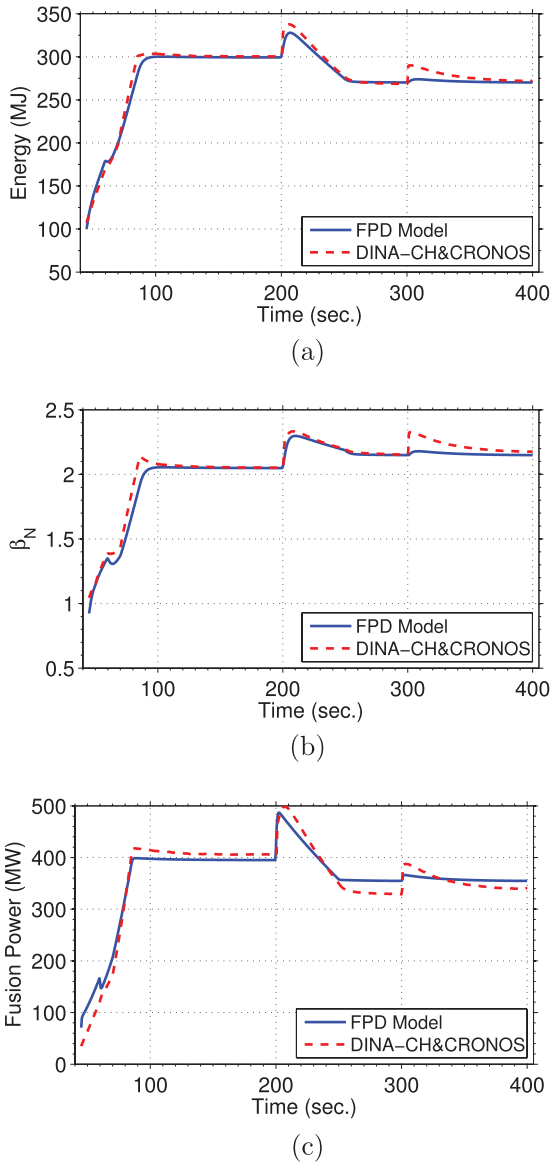


**Figure 8.** (a) Plasma stored energy $\bar{W}$ versus time, (b) plasma normalized beta $\beta_N$ versus time and (c) fusion power $P_{fus}$ versus time.

$$\begin{aligned}\frac{\partial\theta}{\partial t} &= \left[q_{\eta_1} + q_{\eta_4}\delta_{T_e}\right]\frac{\partial^2\theta}{\partial\hat{\rho}^2} + \left[q_{\eta_2} + q_{\eta_5}\delta_{T_e}\right]\frac{\partial\theta}{\partial\hat{\rho}} + \left[q_{\eta_3} + q_{\eta_6}\delta_{T_e}\right]\theta \\ &+ \sum_i \left[g_i' + h_i'\delta_{n_e} + k_i'\delta_{T_e} + l_i'\delta_{T_e}\delta_{n_e} + m_i'\delta_{T_e}^2 + p_i'\delta_{T_e}^2\delta_{n_e}\right]P_i(t) \\ &- \left[g_{bs} + h_{bs}\delta_{n_e} + k_{bs}\delta_{T_e} + l_{bs}\delta_{T_e}\delta_{n_e} + m_{bs}\delta_{T_e}^2 + p_{bs}\delta_{T_e}^2\delta_{n_e}\right]\left(\frac{1}{\theta}\right)^2\frac{\partial\theta}{\partial\hat{\rho}} \\ &+ \left[g_{bs}' + h_{bs}'\delta_{n_e} + k_{bs}'\delta_{T_e} + l_{bs}'\delta_{T_e}\delta_{n_e} + m_{bs}'\delta_{T_e}^2 + p_{bs}'\delta_{T_e}^2\delta_{n_e}\right]\left(\frac{1}{\theta}\right),\end{aligned} \tag{39}$$

with boundary conditions

$$\theta(0,t) = 0 \qquad \theta(1,t) = -k_{I_p}I_p(t), \tag{40}$$

where $i \in \{\mathrm{ec}_1, \mathrm{ec}_2, \mathrm{ec}_3, \mathrm{nbi}\}$, the parameters $q_{\eta_j}(\hat{\rho})$, for $j = 1, \ldots, 6$, $g_i(\hat{\rho})$, $h_i(\hat{\rho})$, $k_i(\hat{\rho})$, $l_i(\hat{\rho})$, $m_i(\hat{\rho})$, $p_i(\hat{\rho})$, $g_{bs}(\hat{\rho})$, $h_{bs}(\hat{\rho})$, $k_{bs}(\hat{\rho})$, $l_{bs}(\hat{\rho})$, $m_{bs}(\hat{\rho})$, $p_{bs}(\hat{\rho})$ are functions of space and $(\cdot)' = \mathrm{d}/\mathrm{d}\hat{\rho}(\cdot)$. See [64] for an detailed derivation of (39). The FPD model (39)–(40) contains the physics information of how the control actuators, as well as the uncertain parameters $\delta_{n_e}$ and $\delta_{T_e}$, influence the poloidal flux gradient profile dynamics, and the goal is to embed the physics into the feedback controller by converting the physics information into a form suitable to synthesize a feedback controller.

### 6.3. Feedback control algorithm synthesis

We begin by seeking a finite dimensional ODE model of the poloidal magnetic flux gradient profile dynamics to facilitate the synthesis of a feedback controller. An approximate ODE model is obtained by spatially discretizing the governing infinite dimensional PDE (39) using a truncated Taylor series expansion while leaving the time domain continuous [65] (see section 4.4). The non-dimensional spatial domain of interest ($\hat{\rho} \in [0, 1]$) is represented as $m_\theta$ discrete nodes, and the spacing between the nodes $\Delta\hat{\rho}$ is defined as $\Delta\hat{\rho} = 1/(m_\theta - 1)$. Central finite difference spatial derivative approximations of order $(\Delta\hat{\rho})^2$ are used in the interior node region, $2 \leqslant i \leqslant (m_\theta - 1)$. After applying the spatial derivative approximations to (39) and taking into account the boundary conditions (40), we obtain a nonlinear approximate finite dimensional ODE model defined by

$$\dot{x} = f_\theta(x, u_q, \delta), \tag{41}$$

where $x = [\theta_2, \theta_3, \ldots, \theta_{m_\theta - 1}]^T \in \mathbb{R}^{n_\theta}$ is the state vector, $\theta_i$ is the value of $\theta$ at the discrete spatial nodes, $u_q = [P_{\mathrm{ec}_1}, P_{\mathrm{ec}_2}, P_{\mathrm{ec}_3}, P_{\mathrm{nbi}}, I_p]^T \in \mathbb{R}^5$ is the control input vector, $\delta = [\delta_{T_e}, \delta_{n_e}, \delta_{T_e}\delta_{n_e}, \delta_{T_e}^2, \delta_{T_e}^2\delta_{n_e}] \in \mathbb{R}^5$ is the uncertain parameter vector, $f_\theta \in \mathbb{R}^{n_\theta}$ is a nonlinear function of the model parameters, the system states, the control inputs and the uncertain parameters, $n_\theta = m_\theta - 2$ and

$$\theta_1(t) = 0 \qquad \theta_{m_\theta}(t) = -k_{I_p}I_p(t).$$

We define a nominal equilibrium point of the system (41) as

$$\dot{x}_{\mathrm{eq}} = f_\theta(x_{\mathrm{eq}}, u_{\mathrm{eq}_q}, 0) = 0. \tag{42}$$

We can obtain a model suitable for tracking control design by defining the perturbation variables $\tilde{x}(t) = x(t) - x_{\mathrm{eq}}$ and $u_{\mathrm{fb}_q}(t) = u_q(t) - u_{\mathrm{eq}_q}$, where $\tilde{x}(t)$ is the deviation away from the equilibrium state and $u_{\mathrm{fb}_q}(t)$ is the output of the to-be-designed feedback controller. Linearizing (41) *with respect to the state and control input* around an equilibrium point defined by (42), we obtain a *linear time-invariant* (LTI) model of the deviation dynamics given by

$$\dot{\tilde{x}} = \left.\frac{\partial f_\theta}{\partial x}\right|_{(x_{\mathrm{eq}}, u_{\mathrm{eq}_q}, \delta)} \tilde{x} + \left.\frac{\partial f_\theta}{\partial u_q}\right|_{(x_{\mathrm{eq}}, u_{\mathrm{eq}_q}, \delta)} u_{\mathrm{fb}_q} + d_\delta, \tag{43}$$

where $\partial f_\theta/\partial x \in \mathbb{R}^{n_\theta \times n_\theta}$ and $\partial f_\theta/\partial u_q \in \mathbb{R}^{n_\theta \times 5}$ are the system Jacobians, which depend on the uncertain parameters $\delta$, and $d_\delta = f_\theta(x_{\mathrm{eq}}, u_{\mathrm{eq}_q}, \delta)$. The model of the deviation dynamics given in (43) can be written in a conventional state-space form as

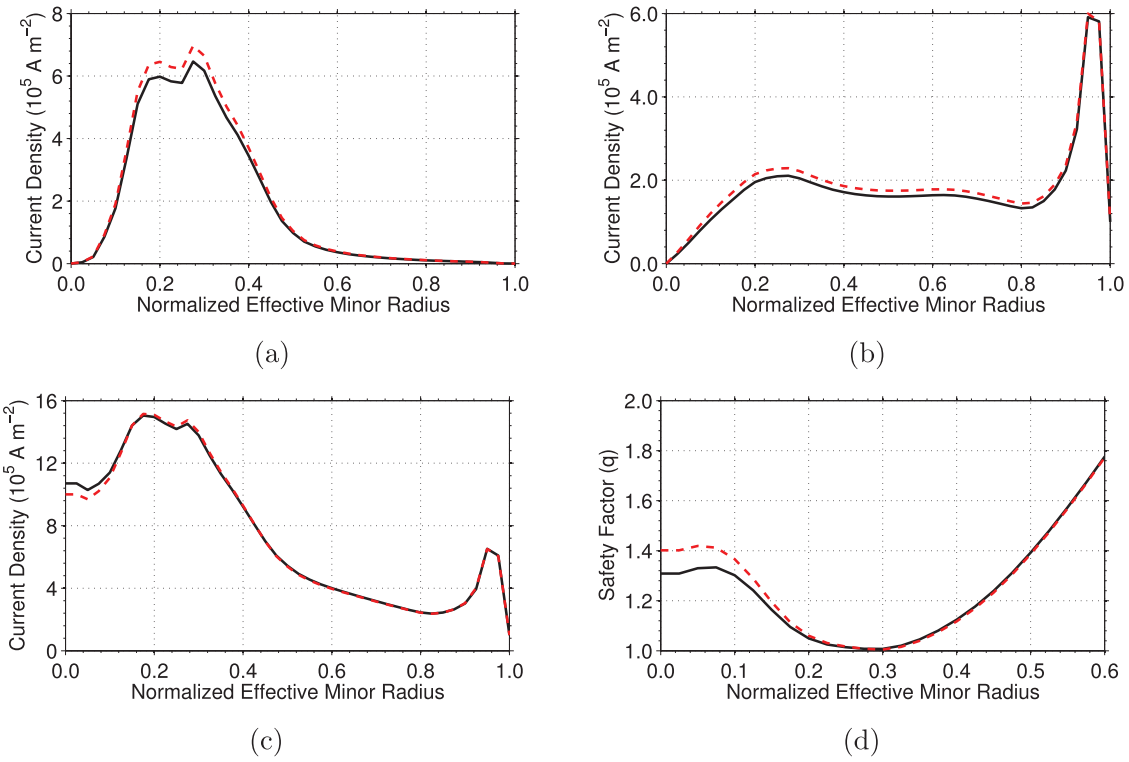


**Figure 9.** Comparison of stationary state plasma parameters in ITER at $I_p = 11$ MA with $P_{ec_1} = P_{ec_2} = P_{ec_3} = 4$ MW, $P_{nbi} = 20$ MW, $\bar{n}_e = 7.35 \times 10^{19}$ m$^{-3}$ and $P_{ic} = 5$ MW (solid) and $P_{ic} = 20$ MW (dash): (a) auxiliary, (b) bootstrap and (c) toroidal current density, respectively and (d) $q$ profile.

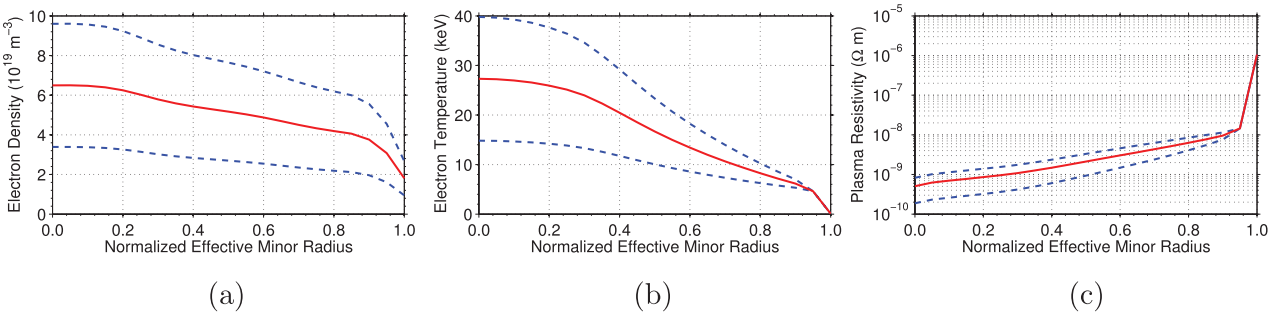


**Figure 10.** Plasma parameter uncertainty ranges in ITER: (a) electron density, (b) electron temperature and (c) plasma resistivity. Note: nominal values (solid) and minimum/maximum values (dash).

$$\begin{aligned} \dot{\tilde{x}} &= A\tilde{x} + Bu_{\mathrm{fb}_q} + d_\delta, \\ y &= C\tilde{x} + Du_{\mathrm{fb}_q}, \end{aligned} \tag{44}$$

with

$$\begin{aligned} A &= A_0 + \sum_{m=1}^{5} \delta_m A_m \qquad B = B_0 + \sum_{m=1}^{5} \delta_m B_m, \\ C &= C_0 + \sum_{m=1}^{5} \delta_m C_m \qquad D = D_0 + \sum_{m=1}^{5} \delta_m D_m, \end{aligned} \tag{45}$$

where $A$ and $B$ are the Jacobians evaluated at $(x_{\mathrm{eq}}, u_{\mathrm{eq}_q}, \delta)$, $A_i$ and $B_i$, for $i = 0, \ldots, 5$ are the component matrices of $A$ and $B$, respectively, $C_0$ is an $n_\theta \times n_\theta$ identity matrix, $D_0 = 0$, and $C_j = 0$ and $D_j = 0$ for $j = 1, \ldots, 5$. Note that this matrix selection implies that $y = \tilde{x}$, which also implies that we assume the plasma magnetic state is measurable and available for feedback control. The state-space system (44)–(45) is referred to as a linear *uncertain* system in the control theory literature, where $A_0$, $B_0$, $C_0$ and $D_0$ represent the nominal system and $A_m$, $B_m$, $C_m$ and $D_m$ represent the influence that each uncertain parameter $\delta_m$ has on the system.

The target plasma state evolution is prescribed by a reference vector $r(t)$ and the control objective is to drive the system output $y(t)$ to the target evolution. Therefore, we define the tracking error $e(t)$ as

$$e(t) = r(t) - y(t). \tag{46}$$

The feedback control objectives are to (i) maintain a small tracking error for any external reference input, (ii) reject the effects of any external disturbance input and (iii) utilize as little feedback control effort as possible. This control problem can be expressed mathematically as

$$\min_{K} \|T_{zw}\|_{\infty}, \tag{47}$$

where $K$ is the feedback controller, the function $T_{zw}$ represents the influence that the external reference and disturbance parameters have on the tracking error and feedback control input in closed-loop and $\|\cdot\|_{\infty}$ denotes the $H_{\infty}$ norm [63]. Note that $T_{zw}$ is dependent on both the system model (44) and the feedback controller $K$. The feedback control objectives imply that we want to minimize the influence that a change in the external reference and disturbance inputs have on the tracking error and feedback control input in closed-loop, i.e. minimize the gain (or norm) of the transfer function $T_{zw}$. The $H_{\infty}$ norm is defined as the maximum gain of a stable transfer function, i.e

$$\|T_{zw}(s)\|_{\infty} = \max_{\omega} \bar{\sigma}(T_{zw}(j\omega)),$$

where $s$ denotes the Laplace variable and $\bar{\sigma}(T_{zw}(j\omega))$ denotes the maximum singular value of the transfer function $T_{zw}$ at each frequency $\omega$. The maximum singular value represents the largest amplification between a stable transfer function's inputs and outputs. Therefore, if we are able to minimize the $H_{\infty}$ norm of $T_{zw}$, we will have minimized the largest amplification that the external reference and disturbance parameters have on the tracking error and feedback control input in closed-loop, thus achieving the feedback control objectives. The safety factor profile feedback controller found by solving the control problem[3] is written in state-space form as

$$\begin{aligned} \dot{x}_{\mathrm{fb}_q} &= A_{\mathrm{fb}_q} x_{\mathrm{fb}_q} + B_{\mathrm{fb}_q} e, \\ u_{\mathrm{fb}_q} &= C_{\mathrm{fb}_q} x_{\mathrm{fb}_q} + D_{\mathrm{fb}_q} e, \end{aligned} \tag{48}$$

where the vector $x_{\mathrm{fb}_q} \in \mathbb{R}^{n_{\mathrm{fb}_q}}$ is the internal controller states, $A_{\mathrm{fb}_q} \in \mathbb{R}^{n_{\mathrm{fb}_q} \times n_{\mathrm{fb}_q}}$, $B_{\mathrm{fb}_q} \in \mathbb{R}^{n_{\mathrm{fb}_q} \times n_{\theta}}$, $C_{\mathrm{fb}_q} \in \mathbb{R}^{5 \times n_{\mathrm{fb}_q}}$ and $D_{\mathrm{fb}_q} \in \mathbb{R}^{5 \times n_{\theta}}$ are the controller system matrices and $n_{\mathrm{fb}_q}$ is the number of $q$ profile controller states. In appendix A, a mathematical derivation of the transfer function $T_{zw}$ (specifically see (A.7)) and the definition of the controller matrices are provided. Additionally, the controller is designed to ensure that the closed-loop system remains stable for all allowable perturbations $\Delta$, i.e. the ranges of the kinetic plasma parameters shown in figure 10, which is referred to as *robust stabilization* of the system in the control theory literature. This analysis is also shown in appendix A.

In the operating scenarios considered in this work, the ion cyclotron launcher is configured to provide only heating power to the plasma. Therefore, we employ the ion cyclotron launcher in a feedforward + feedback scheme, i.e. $P_{\mathrm{ic}} = P_{\mathrm{ic_{ff}}} + P_{\mathrm{ic_{fb}}}$, where $P_{\mathrm{ic_{ff}}}$ and $P_{\mathrm{ic_{fb}}}$ are the feedforward and feedback components, respectively, to control the plasma stored energy. The stored energy feedback controller is expressed in state-space form as

$$\begin{aligned} \dot{x}_{\mathrm{fb}\,\bar{W}} &= e_{\bar{W}}, \\ P_{\mathrm{ic_{fb}}} &= k_{I_{\mathrm{ic}}} x_{\mathrm{fb}\,\bar{W}} + k_{P_{\mathrm{ic}}} e_{\bar{W}}, \end{aligned} \tag{49}$$

where $x_{\mathrm{fb}\,\bar{W}} \in \mathbb{R}^1$ is the internal controller state, $k_{P_{\mathrm{ic}}}$ and $k_{I_{\mathrm{ic}}}$ are the controller gains, $e_{\bar{W}} = \bar{W}_{\mathrm{tar}} - \bar{W}$ is the error in the stored energy and $\bar{W}_{\mathrm{tar}}$ is the target value for the stored energy. Note that (49) represents a proportional-integral controller. In spite of the fixed structure proposed for controller (49), we have followed a model-based control design approach since the gains $k_{P_{\mathrm{ic}}}$ and $k_{I_{\mathrm{ic}}}$ have not been tuned empirically but by employing a pole placement technique that exploits the availability of the dynamic model (27) to guarantee a desired closed-loop behavior of the stored energy $\bar{W}$.

Due to limited actuation capabilities, such as the available amount of auxiliary heating/current-drive power, the feedback control algorithm may drive the actuators to saturation, which could cause undesirable oscillations in the system to develop. Therefore, the feedback algorithm is complemented by and integrated together with an anti-windup scheme [66] to ensure that the closed-loop system remains well-behaved in the presence of actuator magnitude saturation. The anti-windup compensator is designed to keep the total control request

$$u = u_{\mathrm{ff}} + u_{\mathrm{fb}} + u_{\mathrm{aw}},$$

where the components of the control input vector are defined as $u = [P_{\mathrm{ec_1}}, P_{\mathrm{ec_2}}, P_{\mathrm{ec_3}}, P_{\mathrm{nbi}}, I_{\mathrm{p}}, P_{\mathrm{ic}}]^T \in \mathbb{R}^6$, $u_{\mathrm{ff}}$ is the feedforward control component and $u_{\mathrm{aw}}$ is the output of the anti-windup compensator, from significantly deviating from the range of physically achievable actuator values. A schematic of the closed-loop control system structure is shown in figure 11.

## 7. Feedback control algorithm testing through simulation with the first-principles-driven model

In this section, we test the combined feedback control algorithm (48) and (49) augmented with the anti-windup compensator through simulation with the FPD model of the poloidal magnetic flux profile evolution and the volume-averaged energy balance equation described in sections 4 and 5, respectively. As the feedback algorithm is designed for the high performance phase of the discharge, all of the simulations are started just after the plasma transitions from L-mode to H-mode in these particular simulated scenarios during the current ramp-up phase at the time $t_0 = 45$ s. Additionally, in each simulation, the line average electron density evolution is linearly ramped up from an initial value of $\bar{n}_e(t_0) = 2.75 \times 10^{19}$ m$^{-3}$ to a final value of $\bar{n}_e = 7.35 \times 10^{19}$ m$^{-3}$ at $t = 86$ s and then held constant. The combined feedback control algorithm is implemented with a sampling time of 1 s in all of the feedback-controlled simulations, which is on the order of the energy confinement time and significantly smaller than the resistive current diffusion time in ITER. If necessary, the sampling time could straightforwardly be reduced. We now test the reference tracking and disturbance rejection capabilities of the feedback control algorithm, respectively. We emphasize the scenarios studied are not meant to be representative of any one specific standard ITER operating scenario but are meant to determine the ability of the feedback control algorithm to drive the plasma state evolution to a specified *physically achievable* target evolution.

### 7.1. Reference tracking

We now describe the setup for a test conducted to determine the reference tracking capabilities of the feedback

[3] Commercially available software such as Matlab (www.mathworks.com) is available to solve $H_{\infty}$ minimization control problems.

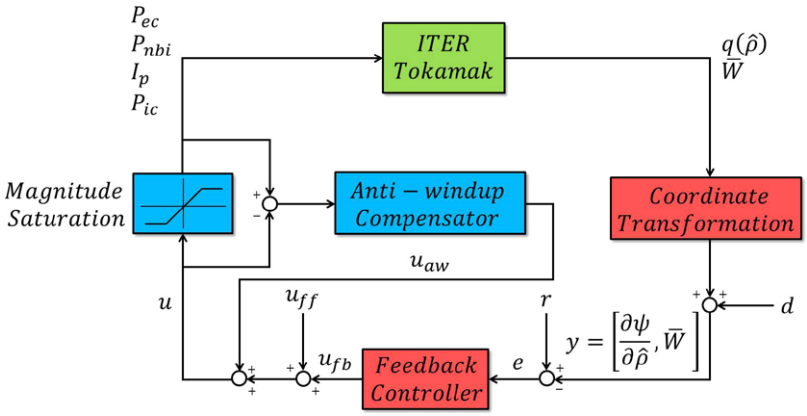


**Figure 11.** Schematic of closed-loop control system structure. The coordinate transformation block converts the simulated plasma parameters to the parameters controlled by the feedback controller ($\theta = \partial\psi/\partial\hat{\rho}$ and $\bar{W}$). The feedback controller reacts to the tracking error and outputs a feedback control request that drives the system in a direction to minimize the tracking error and reject the effects of any external disturbances. The anti-windup compensator reacts to the difference between the saturated and unsaturated actuator requests and outputs an anti-windup control request that minimizes the effects that actuator saturation has on the closed-loop system performance.

algorithm. First, a nominal $q$ profile and stored energy evolution ($q_{\text{nom}}(\hat{\rho}, t)$ and $\bar{W}_{\text{nom}}(t)$) is obtained by executing a feedforward-only simulation with a nominal set of input trajectories and initial conditions. The stationary plasma state reached during this simulation is characterized by a slightly reversed shear $q$ profile with $q_{\min}$ slightly greater than one, a total plasma current of $I_{\text{p}} = 11$ MA, a normalized plasma beta of $\beta_{\text{N}} \approx 2.2$, a fusion power of $P_{\text{fus}} \approx 390$ MW and a total injected auxiliary heating power of $P_{\text{aux}}^{\text{inj}} = 43$ MW. Second, a perturbed $q$ profile and stored energy evolution ($q_{\text{pert}}(\hat{\rho}, t)$ and $\bar{W}_{\text{pert}}(t)$) is obtained by executing a feedforward-only simulation with a perturbed set of input trajectories and initial conditions. Finally, the ability of the feedback algorithm to track a target plasma state evolution, which is obtained from the results of the first simulation, is determined by executing a feedforward + feedback simulation with the perturbed set of input trajectories and initial conditions that are used in the second simulation. The target $q$ profile and stored energy evolution ($q_{\text{tar}}(\hat{\rho}, t)$ and $\bar{W}_{\text{tar}}(t)$) is obtained from the nominal evolution as follows: $q_{\text{tar}}(\hat{\rho}, t) = q_{\text{nom}}(\hat{\rho}, t)$ during the time interval $t \in [45, 1600]$ s and

$$\bar{W}_{\text{tar}}(t) = \begin{cases} \bar{W}_{\text{nom}}(t) & 45\text{–}1000 \text{ s} \\ 275 \text{ MJ}(\beta_{\text{N}} \approx 2.1, P_{\text{fus}} \approx 360 \text{ MW}) & 1000\text{–}1300 \text{ s} \\ 297 \text{ MJ}(\beta_{\text{N}} \approx 2.25, P_{\text{fus}} \approx 410 \text{ MW}) & 1300\text{–}1600 \text{ s} \end{cases} \tag{50}$$

This target plasma state evolution provides the opportunity to test the ability of the feedback controller to both track a nominal plasma state evolution ($t \in [45, 1000]$ s) and maintain a stationary $q$ profile while changing the generated fusion power ($t \in [1000, 1600]$ s).

A comparison of the FPD model predicted target, feedforward + feedback controlled and feedforward controlled $q$ profiles at various times, time traces of $q$ at various normalized effective minor radii and a comparison of the target, feedforward + feedback controlled and feedforward controlled plasma stored energy, normalized beta and fusion power as a function of time are shown in figure 12. The control inputs as a function of time are shown in figure 13. By examining the target plasma state evolution, we see that the time necessary for the plasma to reach an approximately stationary state is about 1000 s. During the feedback-controlled simulation, the initial $q$ profile was lower than the target profile. As shown in the figures, the feedback controller is able to reject the effects of the perturbed initial condition and drive the plasma state evolution to the target evolution during the time interval $t \in [45, 1000]$ s (nominal phase of simulation), which is not accomplished with feedforward-only control. The controller utilizes the neutral beam launchers and the total plasma current to react quickly to $q$ profile tracking errors in the plasma core and near the plasma boundary, respectively. For example, during the feedback-controlled simulation during the time interval $t \in [150, 300]$ s, the $q$ profile in the plasma core (figure 12(g)) evolves below the target, and in response, the controller increases the off-axis neutral beam power (figure 13(d)). Then during the time interval $t \in [300, 600]$ s, the $q$ profile in the plasma core (figure 12(g)) evolves above the target, and in response, the controller decreases the off-axis neutral beam power (figure 13(d)). The controller utilizes the gyrotron launchers more subtly to eliminate more localized $q$ profile tracking errors in the plasma core and the ion cyclotron launcher to eliminate plasma stored energy tracking errors. Additionally, the feedback controller is able to drive (i) the $q$ profile to the target evolution in approximately 400 s in the core region of the plasma (roughly $\hat{\rho} \in [0, 0.4]$) and in approximately 200 s in the outer region of the plasma (roughly $\hat{\rho} \in [0.4, 1]$), and (ii) the thermal plasma state to the target evolution in approximately 75 s. Finally during the time interval $t \in [1000, 1600]$ s, the controller is able to maintain the target stationary $q$ profile while simultaneously changing the generated fusion power. The total plasma current and gyrotron launcher powers reach stationary values during this phase of the simulation. Therefore, the controller utilizes the neutral beam power to counteract the effect that the changing ion

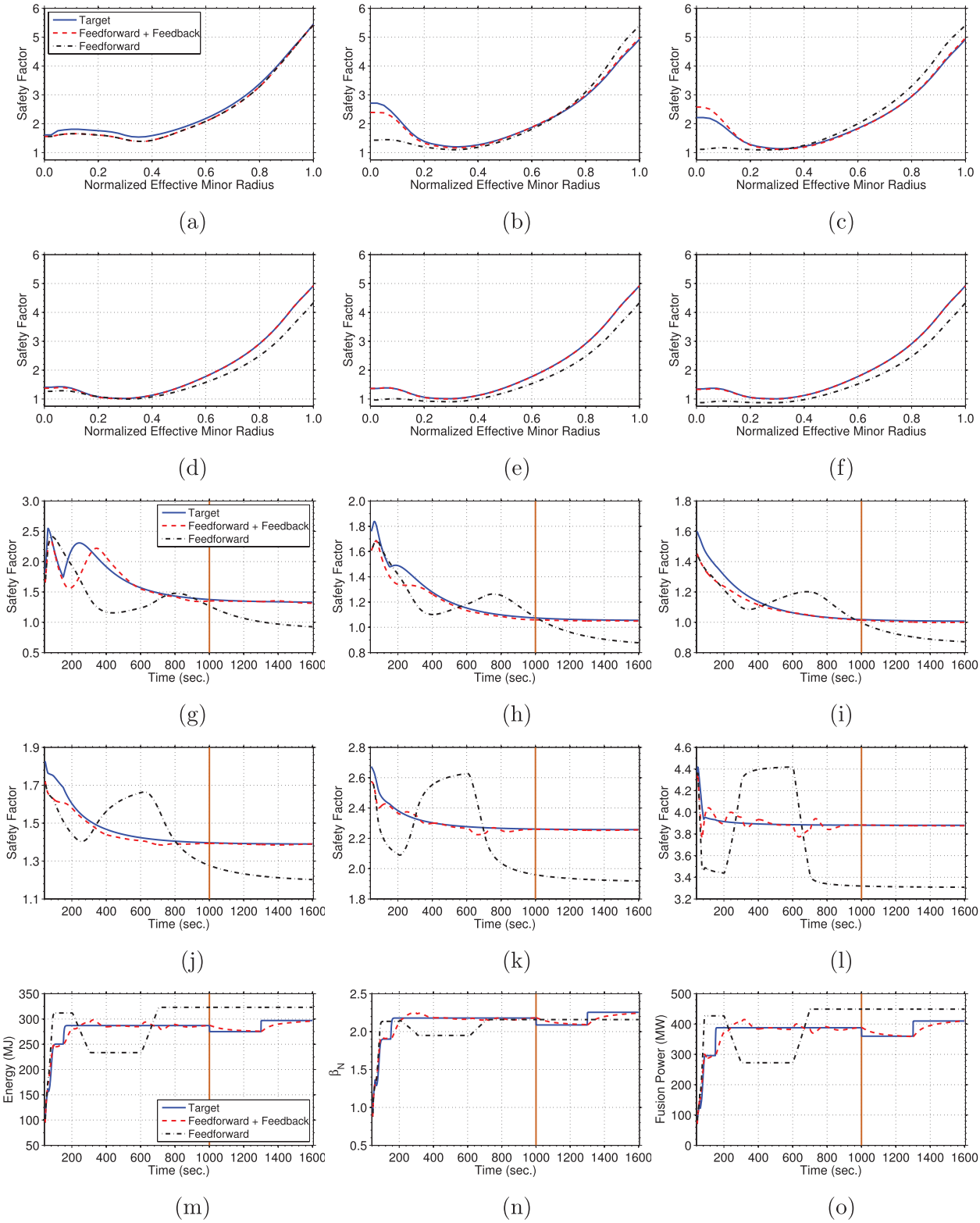


**Figure 12.** (a)–(f) Comparison of target, feedforward + feedback controlled and feedforward controlled $q$ profiles at various times, (g)–(l) time traces of $q$ at various radial locations and (m)–(o) time traces of plasma stored energy, normalized $\beta$ and fusion power for the simulation in section 7.1. The solid-orange line denotes when the target $q$ profile is maintained in a stationary condition while modifying the generated fusion power. (a) $t = 45$ s. (b) $t = 300$ s. (c) $t = 400$ s. (d) $t = 1000$ s. (e) $t = 1300$ s. (f) $t = 1600$ s. (g) $\hat{\rho} = 0.1$. (h) $\hat{\rho} = 0.2$. (i) $\hat{\rho} = 0.3$. (j) $\hat{\rho} = 0.5$. (k) $\hat{\rho} = 0.7$. (l) $\hat{\rho} = 0.9$. (m) $\bar{W}(t)$. (n) $\beta_N(t)$. (o) $P_{fus}(t)$.

cyclotron power (pure plasma heating to track the target thermal plasma state) has on the $q$ profile, i.e. a lower ion cyclotron power results in a lower bootstrap current and a lower total auxiliary current (shown in section 6.1) and as a result a higher neutral beam power is needed to maintain a stationary $q$ profile and vice versa.

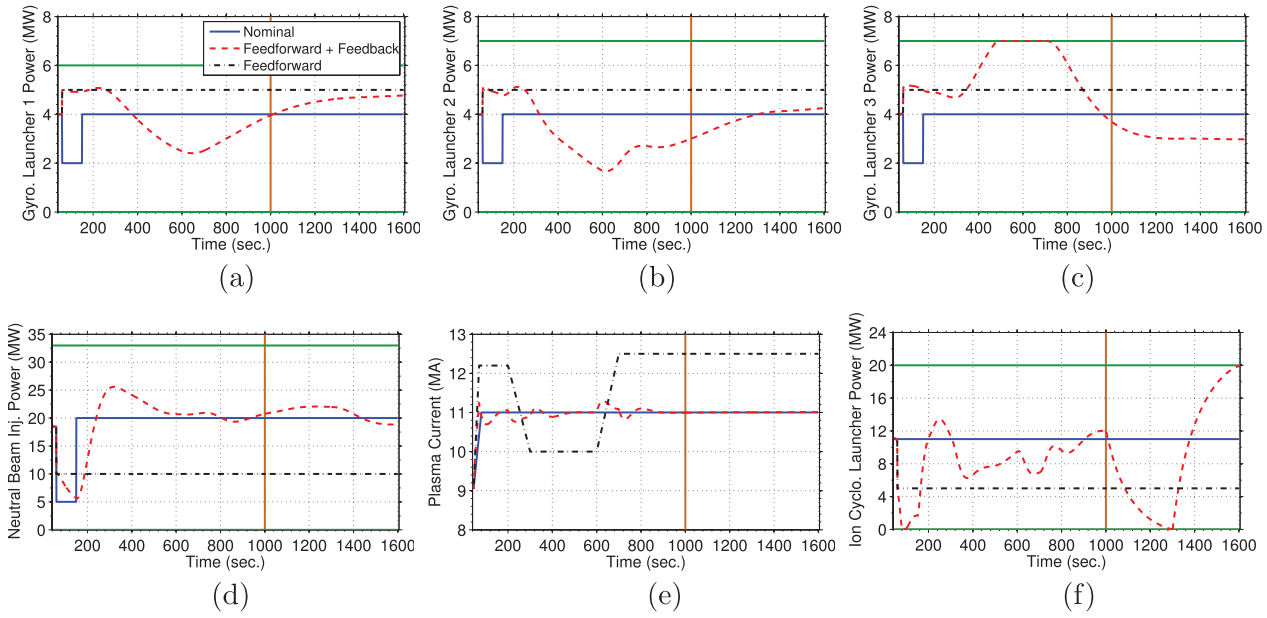


**Figure 13.** Control actuator trajectory comparison for simulation in section 7.1: (a)–(c) individual gyrotron launcher powers, (d) neutral beam injection power, (e) total plasma current and (f) ion cyclotron launcher power. The actuator magnitude limits are shown in solid-green. The solid-orange line denotes the time when the target $q$ profile is maintained in a stationary condition while modifying the generated fusion power. (a) $P_{\mathrm{ec}_1}(t)$. (b) $P_{\mathrm{ec}_2}(t)$. (c) $P_{\mathrm{ec}_3}(t)$. (d) $P_{\mathrm{nbi}}(t)$. (e) $I_{\mathrm{p}}(t)$. (f) $P_{\mathrm{ic}}(t)$.

### *7.2. Disturbance rejection*

As in the reference tracking simulation study, a nominal $q$ profile and stored energy evolution ($q_{\mathrm{nom}}(\hat{\rho},t)$ and $\bar{W}_{\mathrm{nom}}(t)$) is first obtained by executing a feedforward-only simulation with a nominal set of input trajectories and initial conditions. The stationary plasma state reached during this simulation is characterized by a moderately reversed shear $q$ profile with $q_{\min}$ slightly greater than one, a total plasma current of $I_{\mathrm{p}} = 10.5$ MA, a normalized plasma beta of $\beta_{\mathrm{N}} \approx 2.3$, a fusion power of $P_{\mathrm{fus}} \approx 410$ MW and a total injected auxiliary heating power of $P_{\mathrm{aux}}^{\mathrm{inj}} = 62$ MW. A perturbed $q$ profile and stored energy evolution ($q_{\mathrm{pert}}(\hat{\rho},t)$ and $\bar{W}_{\mathrm{pert}}(t)$) is later obtained by executing a feedforward-only simulation with a perturbed set of input trajectories and initial conditions. Finally, the ability of the algorithm to track a target plasma state evolution, which is obtained from the results of the first simulation, is determined by executing a feedforward + feedback simulation with the perturbed set of input trajectories and initial conditions that are used in the second simulation. The target $q$ profile and stored energy evolution ($q_{\mathrm{tar}}(\hat{\rho},t)$ and $\bar{W}_{\mathrm{tar}}(t)$) is obtained from the nominal evolution as follows: $q_{\mathrm{tar}}(\hat{\rho},t) = q_{\mathrm{nom}}(\hat{\rho},t)$ during the time interval $t \in [45, 1600]$ s and

$$\bar{W}_{\mathrm{tar}}(t) = \begin{cases} \bar{W}_{\mathrm{nom}}(t) & 45\text{–}1000\ \mathrm{s} \\ 275\ \mathrm{MJ}(\beta_{\mathrm{N}} \approx 2.2, P_{\mathrm{fus}} \approx 370\ \mathrm{MW}) & 1000\text{–}1300\ \mathrm{s} \\ 297\ \mathrm{MJ}(\beta_{\mathrm{N}} \approx 2.35, P_{\mathrm{fus}} \approx 420\ \mathrm{MW}) & 1300\text{–}1600\ \mathrm{s} \end{cases} \tag{51}$$

During the feedback-controlled simulation, the feedback controller is turned on and off during the simulation according to

$$u_{\mathrm{fb}} = \begin{cases} 45\text{–}300\ \mathrm{s} & \mathrm{ON} \\ 300\text{–}500\ \mathrm{s} & \mathrm{OFF}, \\ 500\text{–}1600\ \mathrm{s} & \mathrm{ON} \end{cases} \tag{52}$$

to introduce a disturbance in the plasma state evolution and to determine the ability of the feedback controller to reject such a disturbance and regulate the plasma state evolution around the target trajectories. This is a common practice in plasma control experiments because this emulates dramatic disturbances in the state, i.e. the plasma evolves driven by the feedforward input, that cannot be achieved by input disturbances alone, which are usually quickly rejected by the feedback controller without affecting much the plasma state.

A comparison of the FPD model predicted target, feedforward + feedback controlled and feedforward controlled $q$ profiles at various times, time traces of $q$ at various normalized effective minor radii and a comparison of the target, feedforward + feedback controlled and feedforward controlled plasma stored energy, normalized beta and fusion power as a function of time are shown in figure 14. The control inputs as a function of time are shown in figure 15. By examining the target plasma state evolution, we see that the time necessary for the plasma to reach an approximately stationary state is again about 1000 s. During the feedback-controlled simulation, the initial $q$ profile was higher than the target profile. As shown in the figures, the feedback controller is able to reject the effects of the perturbed initial condition and drive the $q$ profile and plasma stored energy evolutions towards the desired target evolutions before the feedback controller is turned off at 300 s. During the time interval when the feedback controller is off in the feedback-controlled simulation ($t \in [300, 500]$ s), the plasma state evolves away from the target evolution towards the feedforward-only-controlled plasma state evolution. Once the feedback controller is turned on again at 500 s, it is once again able to drive the plasma state evolution towards the target evolution, which is not accomplished with feedforward-only control. The controller utilizes the actuators to control the plasma state in the same manner

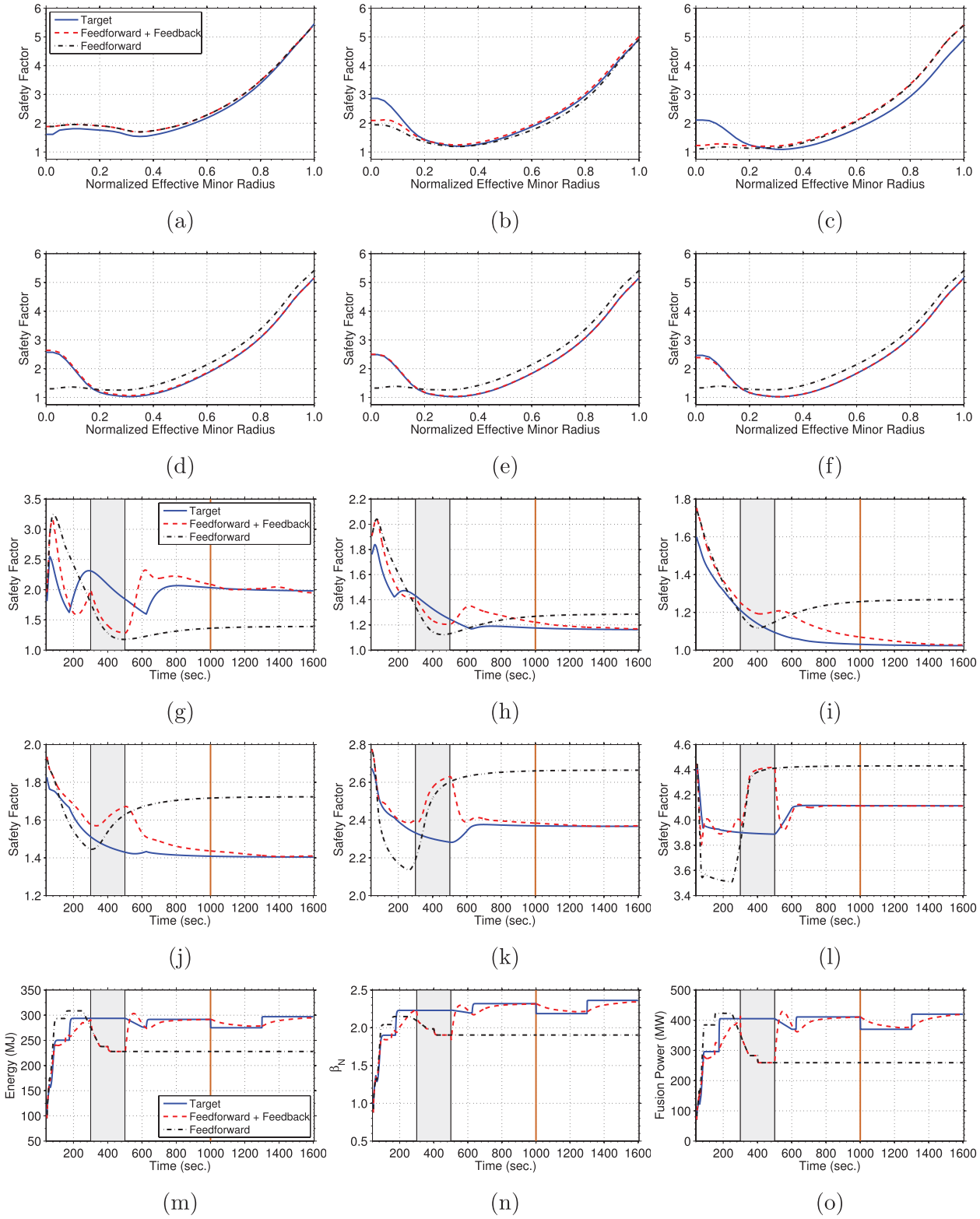


**Figure 14.** (a)–(f) Comparison of target, feedforward + feedback controlled and feedforward controlled $q$ profiles at various times, (g)–(l) time traces of $q$ at various radial locations and (m)–(o) time traces of plasma stored energy, normalized $\beta$ and fusion power for the simulation in section 7.2. The shaded gray region denotes when the feedback controller is not active. The solid-orange line denotes when the target $q$ profile is maintained in a stationary condition while modifying the generated fusion power. (a) $t = 45$ s {FB–ON}. (b) $t = 300$ s {FB–ON}. (c) $t = 500$ s {FB–OFF}. (d) $t = 1000$ s {FB–ON}. (e) $t = 1300$ s {FB–ON}. (f) $t = 1600$ s {FB–ON}. (g) $\hat{\rho} = 0.1$. (h) $\hat{\rho} = 0.2$. (i) $\hat{\rho} = 0.3$. (j) $\hat{\rho} = 0.5$. (k) $\hat{\rho} = 0.7$. (l) $\hat{\rho} = 0.9$. (m) $\bar{W}(t)$. (n) $\beta_N(t)$. (o) $P_{fus}(t)$.

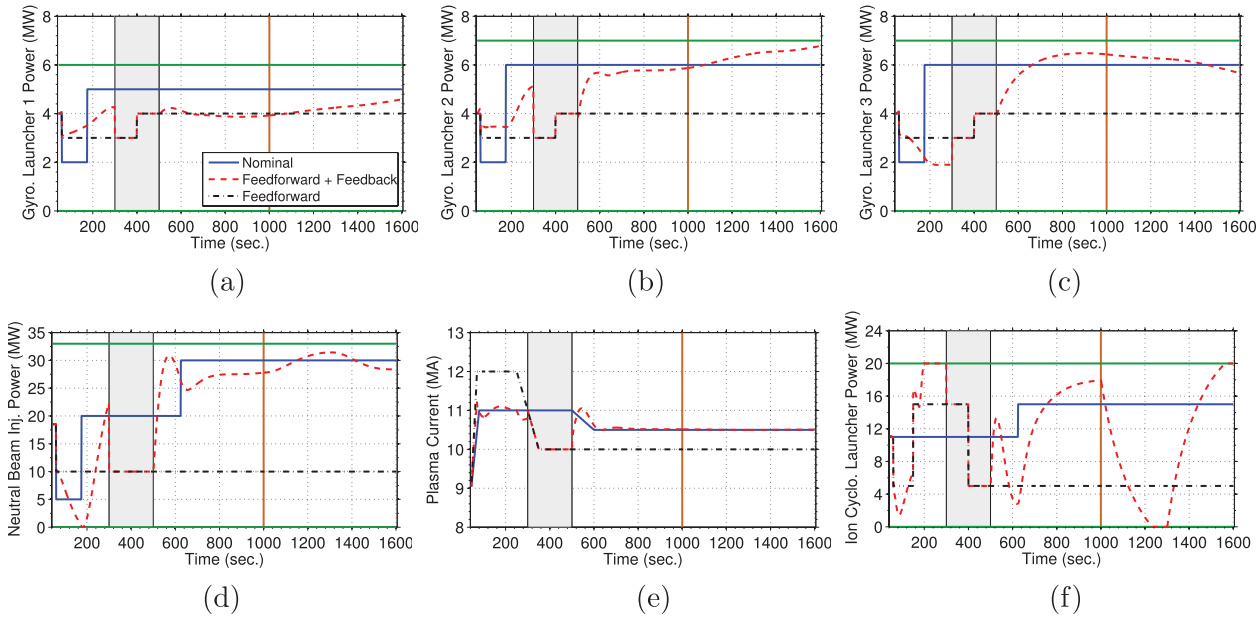


**Figure 15.** Control actuator trajectory comparison for simulation in section 7.2: (a)–(c) individual gyrotron launcher powers, (d) neutral beam injection power, (e) total plasma current and (f) ion cyclotron launcher power. The shaded gray region denotes when the feedback controller is not active. The actuator magnitude limits are shown in solid-green. The solid-orange line denotes the time when the target $q$ profile is maintained in a stationary condition while modifying the generated fusion power. (a) $P_{\mathrm{ec}_1}(t)$. (b) $P_{\mathrm{ec}_2}(t)$. (c) $P_{\mathrm{ec}_3}(t)$. (d) $P_{\mathrm{nbi}}(t)$. (e) $I_{\mathrm{p}}(t)$. (f) $P_{\mathrm{ic}}(t)$.

as observed in section 7.1, i.e. the neutral beam launchers and total plasma current to react quickly to $q$ profile tracking errors in the plasma core and near the plasma boundary, respectively, and the gyrotron launchers more subtly to eliminate localized $q$ profile tracking errors in the plasma core and the ion cyclotron launcher to eliminate plasma stored energy tracking errors. Additionally, the feedback controller is able to drive the plasma state to the target evolution in approximately the same amount of time as observed in section 7.1. Finally during the time interval $t \in [1000, 1600]$ s, the controller is able to maintain the target stationary $q$ profile while simultaneously changing the generated fusion power in the same manner as observed in section 7.1.

## 8. Conclusion and discussion

A general control-oriented physics-based modeling approach to obtain *first-principles-driven* models of the plasma magnetic profile and stored energy evolutions valid for H-mode, high performance plasma scenarios in the tokamak was developed. The FPD model was tailored to H-mode burning plasma scenarios in the ITER tokamak by employing the DINA-CH & CRONOS [5–9] free-boundary tokamak simulation code, and the FPD model's prediction capabilities were demonstrated by comparing the prediction to data obtained from the simulation code. A physics-model-based feedback control algorithm was designed to track target $q$ profile and stored energy evolutions in H-mode burning plasma scenarios in ITER. The feedback controller was designed by embedding a FPD model of the plasma magnetic profile evolution into the control design process and to be *robust* to uncertainties in the electron density, electron temperature and plasma resistivity profiles, which provides some additional confidence that the algorithm can maintain closed-loop system stability in a variety of operating conditions. Additionally, the feedback controller is a computationally robust and efficient algorithm as it can be computed by a simple matrix multiplication of the controller matrices with the respective tracking errors, which is also advantageous for application in ITER from a computational point-of-view relative to other profile control algorithms that require real-time computation of various plasma profiles [41]. The feedback control algorithm was then successfully tested in reference tracking and disturbance rejection simulations with the developed FPD model of the plasma magnetic profile and stored energy evolution. The demonstrated ability of the feedback controller to (i) drive the system to multiple different operating points and (ii) maintain the $q$ profile at a stationary target (to maintain plasma stability) while modulating the thermal state of the plasma (to respond to changing power demand) is a capability that would be advantageous for application on ITER and eventually, a commercial, power producing tokamak reactor.

As shown by the feedback-controlled simulations, the feedback controller augmented with the anti-windup compensator is able to drive the $q$ profile and plasma stored energy to the target evolutions during both the transient and stationary-state phases of the simulations. The feedback control algorithm uses (i) the gyrotron launchers and the neutral beam injectors to control the $q$ profile near the center of the plasma and the total plasma current to control the $q$ profile near the plasma boundary, as well as account for the effects that the ion cyclotron launcher has on the electron temperature profile, which couples to the $q$ profile evolution through the plasma resistivity, auxiliary current-drive efficiency and bootstrap

current-drive, and (ii) the ion cyclotron launcher to control, and account for the effects that the other actuators have on, the stored energy evolution. The feedback control algorithm could be implemented in existing tokamak experiments by interfacing it with real-time measurements of the $q$ profile and stored energy, respectively. These quantities can be obtained from a real-time Grad-Shafranov equation solver, such as real-time EFIT [67]. An example of how these measurements can be interfaced with the feedback controller can be found in [29]. Additionally, the control algorithm designed in this work represents a second layer of control in the overall scheme utilized to control the tokamak plasma, i.e the actuator requests generated by the controller represent the reference values to the dedicated control loops commanding the physical actuators. Therefore, the control algorithm would also need to be interfaced with the dedicated control loops, for example a dedicated PF coil controller that is designed to track a desired total plasma current request.

Active feedback control of the $q$ profile evolution will be crucial to reject the effects any external disturbances have on the plasma evolution, maintain the plasma in a stable MHD state and maximize the performance of the plasma in ITER. As demonstrated, the feedback controller is able to drive the $q$ profile to the target evolution in approximately 400 s in the core region of the plasma and approximately 200 s in the outer region of the plasma. In the scenarios considered in this work, the auxiliary current-drive sources (gyrotron and neutral beam launchers) are configured to inject power into the plasma away from the magnetic axis as shown in figure 1(f). Therefore, there is no direct way to control the $q$ profile near the magnetic axis, which consequently contributes to the longer response time in the core region of the plasma relative to the outer region. Configuring the neutral beam launchers to inject power into the plasma both on-and-off axis would allow the $q$ profile feedback controller to moderate the relative location of the noninductively-driven current in the plasma. This additional degree of control freedom may possibly allow for tighter control of the $q$ profile, as well as reduce the response time, in the core region of the plasma.

As the $q$ profile portion of the combined feedback controller is designed to be robust to a range of kinetic plasma parameters, detailed real-time knowledge of these kinetic plasma profile evolutions may not be needed to actively control the $q$ profile evolution, which is also advantageous for application in ITER and future reactors by requiring a smaller number of real-time diagnostics relative to other profile control algorithms [41, 54, 56]. Therefore, a separate dedicated control algorithm to control the thermal state of the plasma can be combined together with the $q$ profile feedback controller, as long as the electron density, electron temperature and plasma resistivity profiles remain inside the ranges for which the $q$ profile feedback controller ensures the closed-loop system remains stable. In this work, a proportional-integral feedback controller that utilizes the ion cyclotron launcher was designed to control the plasma stored energy evolution. However, if the ion cyclotron power request is driven to saturation by the feedback controller, then the thermal state of the plasma is no longer controllable using this lone actuator. A subject of future work will be to (i) interface the $q$ profile controller with a nonlinear burn controller [68] that utilizes not only auxiliary heating, but also the concept of isotopic fuel tailoring [69] and impurity injection to control the thermal state of the plasma and (ii) test the control algorithms in closed-loop simulations with the simulation code. In this work, the performance of the linear feedback controller was demonstrated through simulations with the developed nonlinear FPD model. Closed-loop simulations with the more complex simulation code will be key to further validate the ability of the linear controller to control the nonlinear system.

Finally, we have investigated many key practical issues for plasma profile control in ITER, which will be useful for the development of the ITER PCS that has recently been initiated. One of the more critical issues is whether current profile and internal energy control can be achieved through the combination of separate individual control algorithms or whether a more fully integrated approach is required. As shown in the presented feedback-controlled simulations, it appears that the combination of separate control algorithms may be able to achieve the plasma control performance requirements in ITER, as long as the algorithms remain *robust* to changes in the plasma parameters they are not specifically designed to control and the target plasma state is *physically achievable*. However, this may no longer be valid as the number of control objectives increases (e.g. rotation profile control, burn control, etc) and a more fully integrated control design approach could be needed in combination with actuator sharing strategies. Moreover, in order for candidate control solutions to truly be considered for application on ITER, they need to be developed and routinely used in existing tokamak experiments. In [49, 64, 70], the FPD model of plasma magnetic profile and stored energy evolutions developed in this work has been tailored to H-mode scenarios in the DIII-D tokamak. Firstly, this model has been utilized to numerically design actuator trajectories that steer the plasma state through the tokamak operating space to reach a target operating state (feedforward control design) with the objective of supporting the traditional trial-and-error experimental process of advanced scenario planning in DIII-D [48, 49, 64, 71]. Secondly, it has been employed to develop model-based feedback control algorithms to control the $q$ profile and stored energy evolutions in DIII-D H-mode scenarios [49, 64, 71–75]. Experimental testing of these algorithms in DIII-D is a subject of ongoing and future work.

## Acknowledgments

This work was supported by the NSF CAREER award program (ECCS-0645086), the US Department of Energy (DE-SC0001334 and DE-SC0010661) and the Fonds National Suisse de la Recherche Scientifique.

## Appendix A. Mathematical derivation of safety factor profile feedback control algorithm

In this appendix we provide a mathematical derivation of the $q$ profile feedback controller. The uncertain state-space system (44) and (45) is first rewritten into what is referred

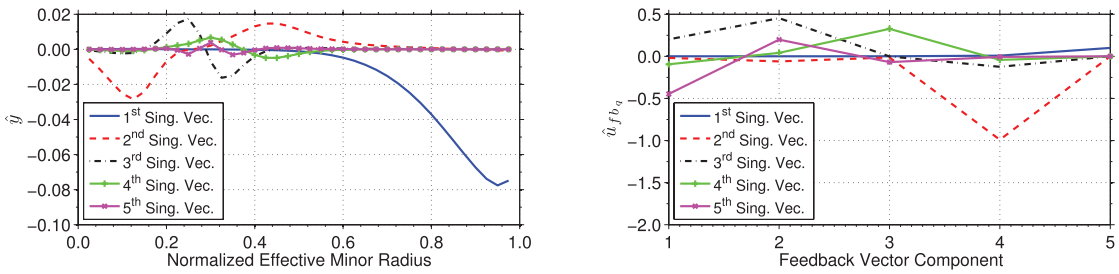


**Figure A1.** Relevant control channels identified with $\omega_{dc} = 0.1$ rad s$^{-1}$: (a) output and (b) input. Note that the components of the control input vector are defined as $u_q = [P_{ec_1}, P_{ec_2}, P_{ec_3}, P_{nbi}, I_p]$.

to as a *robust control framework* in the control theory literature. Secondly, the relevant input–output control channels are identified by employing a singular value decomposition of the nominal input–output relation. Finally, the *robust* feedback controller is designed to track a target $q$ profile evolution.

### A.1. Finite dimensional model in robust control framework

The relationship between the inputs and outputs of a linear state-space system is given by the transfer function of the system $G(s)$, i.e. $y = G(s)u_{fb_q}$ where $G(s) = C(sI_{n_\theta} - A)^{-1}B + D$, $I_{n_\theta}$ is an $n_\theta \times n_\theta$ identity matrix and $s$ denotes the Laplace variable. We note that the nominal model will be coupled with the uncertain parameters in the transfer function representation of the uncertain system (44) and (45). As a result, we group the uncertain parameters into a *block-diagonal structured* uncertainty matrix $\Delta = \text{diag}\{\delta_{T_e}, \delta_{n_e}\}$ and write the system in the conventional $P - \Delta$ control framework (shown in the light purple box in figure A3) by employing the method outlined in [76], where $P(s)$ is the generalized transfer function of the system, in order to separate the uncertain parameters from the nominal parameters. See [29, 64] for an example of this technique. If the transfer function $P \in \mathbb{R}^{(q_T+n_\theta)\times(q_T+5)}$, where $q_T$ is the rank of the uncertainty matrix $\Delta$, is partitioned as

$$P = \begin{bmatrix} P_{11} & P_{12} \\ P_{21} & P_{22} \end{bmatrix},$$

the input–output equations of the system in this framework are

$$\begin{aligned} y_\Delta &= P_{11}u_\Delta + P_{12}u_{fb_q}, \\ y &= P_{21}u_\Delta + P_{22}u_{fb_q} + d, \end{aligned} \tag{A.1}$$

where $P_{11} \in \mathbb{R}^{q_T \times q_T}$, $P_{12} \in \mathbb{R}^{q_T \times 5}$, $P_{21} \in \mathbb{R}^{n_\theta \times q_T}$, $P_{22} \in \mathbb{R}^{n_\theta \times 5}$, $y_\Delta \in \mathbb{R}^{q_T}$, $u_\Delta \in \mathbb{R}^{q_T}$, $y \in \mathbb{R}^{n_\theta}$, $d \in \mathbb{R}^{n_\theta}$ and $u_{fb_q} \in \mathbb{R}^5$. The parameter $d$ represents the effect that the disturbance $d_\delta$ has on the system outputs. The relationship between the generalized transfer function $P(s)$, the uncertainty matrix $\Delta$ and the transfer function $G(s)$ is given by

$$G(s) = P_{22}(s) + P_{21}(s)\Delta[I_{q_T} - P_{11}(s)\Delta]^{-1}P_{12}(s), \tag{A.2}$$

where $I_{q_T}$ is a $q_T \times q_T$ identity matrix. By examining (A.2), we see that the transfer function $P_{22}$ describes the nominal response of the system and that the transfer functions $P_{11}$, $P_{12}$ and $P_{21}$ describe how the uncertain parameters affect the system.

### A.2. Identification of relevant control channels

As the number of outputs ($n_\theta$) is larger than the number of inputs (5), the conditions to bring the tracking error (46) exactly to zero are typically not met. Since the controller is designed based on a linear system that has five control inputs, only five linear combinations of the output of the system can be independently controlled. In this work, we employ a singular value decomposition (SVD) of the nominal state-space system $A_0$, $B_0$, $C_0$, $D_0$ at a particular frequency to evaluate and decouple the most relevant input–output control channels. Therefore, as a result of the limited number of control inputs, the controller will only be able to control the components of the system output that are spanned by the five components of the output SVD basis, which is derived below.

The relationship between the outputs $y$ and inputs $u_{fb_q}$ of the nominal linear state-space system is given by the transfer function of the system which is expressed as $y = G_0(s)u_{fb_q}$, where $G_0(s) = C_0(sI_{n_\theta} - A_0)^{-1}B_0 + D_0$ is the nominal transfer function. The real approximation of the nominal input–output relation at a particular frequency $j\omega_{dc}$ is expressed as

$$\hat{y} = \hat{G}_0\hat{u}_{fb_q}, \tag{A.3}$$

where $\hat{y}$ denotes the relevant output, $\hat{u}_{fb_q}$ denotes the relevant input and $\hat{G}_0$ denotes the real approximation of the complex matrix $G_0(j\omega_{dc})$ [63, 77]. We now introduce the symmetric positive definite weighting matrices $Q \in \mathbb{R}^{n_\theta \times n_\theta}$ and $R \in \mathbb{R}^{5\times 5}$. These weighting matrices allow the designer to weight which parts of the system output are desired to be controlled to achieve the physics objectives (through the selection of $Q$) and which control inputs are desired to be used to achieve these objectives (through the selection of $R$). We next define the 'weighted' nominal transfer function $\tilde{G}_0$ and its economy size (zero rows of $\Sigma$ are eliminated and unnecessary columns of $U$ are not computed) singular value decomposition [78] as

$$\tilde{G}_0 = Q^{1/2}\hat{G}_0R^{-1/2} = U\Sigma V^T,$$

where $\Sigma = \text{diag}(\sigma_1, \sigma_2, \sigma_3, \sigma_4, \sigma_5) \in \mathbb{R}^{5\times 5}$ is a diagonal matrix of singular values and $U \in \mathbb{R}^{n_\theta \times 5}$ and $V \in \mathbb{R}^{5\times 5}$ are matrices that possess the following properties $V^TV = VV^T = I$, $U^TU = I$,

where $I$ is a $5 \times 5$ identity matrix and $(\cdot)^T$ denotes the matrix transpose. The input–output relation (A.3) is now expressed as

$$\hat{y} = Q^{-1/2}\tilde{G}_0 R^{1/2}\hat{u}_{\mathrm{fb}_q} = Q^{-1/2}U\Sigma V^T R^{1/2}\hat{u}_{\mathrm{fb}_q}. \quad \text{(A.4)}$$

The columns of the matrix $Q^{-1/2}U\Sigma$ define a basis for the subspace of obtainable output values, and as a result, any obtainable output can be written as a linear combination $\hat{y}^* \in \mathbb{R}^5$ of the basis vectors, i.e.

$$\hat{y} = Q^{-1/2}U\Sigma\hat{y}^* \Longleftrightarrow \hat{y}^* = \Sigma^{-1}U^T Q^{1/2}\hat{y}. \quad \text{(A.5)}$$

This implies only the component of the reference vector $r$ which also lies in this subspace will be able to be tracked in steady state. As a result, we decompose the reference vector into a trackable component $\hat{r}_t$ and a non-trackable component $r_{nt}$, i.e. $r = \hat{r}_t + r_{nt}$. As the trackable component lies in the subspace of obtainable output values it can also be written as a linear combination $\hat{r}^* \in \mathbb{R}^5$ of the basis vectors, i.e.

$$\hat{r}_t = Q^{-1/2}U\Sigma\hat{r}^* \Longleftrightarrow \hat{r}^* = \Sigma^{-1}U^T Q^{1/2}(\hat{r}_t + r_{nt}), \quad \text{(A.6)}$$

where $\Sigma^{-1}U^T Q^{1/2} r_{nt} = 0$ because the non-trackable component does not lie in the obtainable output subspace. By defining

$$\hat{u}^*_{\mathrm{fb}_q} = V^T R^{1/2}\hat{u}_{\mathrm{fb}_q} \Longleftrightarrow \hat{u}_{\mathrm{fb}_q} = R^{-1/2}V\hat{u}^*_{\mathrm{fb}_q},$$

where $\hat{u}^*_{\mathrm{fb}_q} \in \mathbb{R}^5$, a one-to-one relationship between $\hat{y}^*$ and $\hat{u}^*_{\mathrm{fb}_q}$ is obtained by using (A.5) and (A.4) as

$$\begin{aligned}\hat{y}^* &= \Sigma^{-1}U^T Q^{1/2}\hat{y} \\ &= \Sigma^{-1}U^T Q^{1/2}Q^{-1/2}U\Sigma V^T R^{1/2}\hat{u}_{\mathrm{fb}_q} = \hat{u}^*_{\mathrm{fb}_q}.\end{aligned}$$

By utilizing (A.6) and (A.5), the tracking error (46) is now written as

$$\hat{e} = \hat{r} - \hat{y} = Q^{-1/2}U\Sigma(\hat{r}^* - \hat{y}^*).$$

The singular vectors of the basis for the subspace of obtainable output values $Q^{-1/2}U\Sigma$ are shown in figure A1(a), and the corresponding input singular vectors $R^{-1/2}V$ are shown in figure A1(b). As the magnitude of the singular value $\sigma_i$ decreases, a larger amount of control effort is needed along the direction of the associated input singular vector to produce a significant contribution to the profile in the direction of the associated output singular vector. Therefore, to avoid spending a lot of control effort for only a small improvement in value of the tracking error, we can partition the singular values into $k_s$ significant singular values $\Sigma_s$ and $5 - k_s$ negligible singular values $\Sigma_{ns}$ and define the significant components of the reference, output and input vectors as

$$\begin{aligned}\hat{r}^*_s &= \Sigma_s^{-1}U_s^T Q^{1/2}(\hat{r}_t + r_{nt}) \in \mathbb{R}^{k_s}, \\ \hat{y}^*_s &= \Sigma_s^{-1}U_s^T Q^{1/2}\hat{y} \in \mathbb{R}^{k_s}, \\ \hat{u}^*_{\mathrm{fb}_{q_s}} &= V_s^T R^{1/2}\hat{u}_{\mathrm{fb}_q} \in \mathbb{R}^{k_s},\end{aligned}$$

where $U_s \in \mathbb{R}^{n_\theta \times k_s}$ and $V_s \in \mathbb{R}^{5\times k_s}$ are the components of $U$ and $V$ associated with the significant singular values.

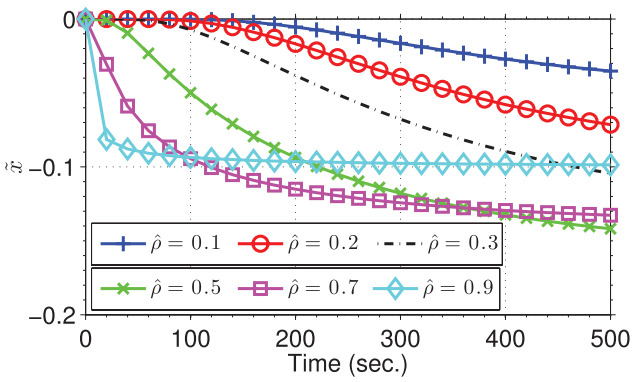


**Figure A2.** Response of the nominal state-space system $y = \tilde{x} = G_0(s)u_{\mathrm{fb}_q}$ to a 1 MA step input in the plasma current. The system response is much faster near the plasma boundary compared to the response in the plasma core. The equilibrium state around which the dynamics are linearized is the state achieved at 400 s in the simulation shown in section 5.2.

It is a common practice to consider evaluating the relevant channels at a stationary state, i.e. $\omega_{\mathrm{dc}} = 0$ rad s$^{-1}$. Figure A2 shows the response of the nominal system $y = G_0(s)u_{\mathrm{fb}_q}$ to a 1 MA step input in the total plasma current. As shown in the figure, the response of the system is much slower in the plasma core compared to the response of the system near the plasma boundary. Therefore, evaluating the relevant control channels at a stationary state, i.e. using the total plasma current to control the $q$ profile across the entire spatial domain, could lead to an undesirable transient closed-loop system response because the control action applied at the plasma boundary takes a significant amount of time to diffuse to the plasma core. As a result, we select the frequency as $\omega_{\mathrm{dc}} = 10^{-1}$ rad s$^{-1}$, which allows us to utilize the total plasma current to control the $q$ profile near the plasma boundary and the gyrotron launchers and the neutral beam injectors to control the $q$ profile in the plasma core. This can be seen from the singular vectors shown in figure A1. First, in figure A1(b), the 1st singular vector (blue solid line) only has a non-zero contribution from the 5th feedback vector component, which is the total plasma current. The influence that this control input direction has on the system output is shown in figure A1(a) by the 1st singular vector (blue solid line). This output direction only has non-zero contributions for $\hat{\rho} > 0.5$. Therefore, the 1st singular vector allows the use of $I_p$ to control the $q$ profile near the plasma boundary and not in the plasma core. A similar analysis shows that the 2nd singular vector (red dashed line) has a large contribution from the 4th feedback vector component, which are the neutral beam injectors. The influence that this control input direction has on the system output is shown in figure A1(a) by the 2nd singular vector (red dashed line). Therefore, the neutral beam injectors are used to control the $q$ profile in the spatial region $0 < \hat{\rho} < 0.7$. Finally, the 3rd–5th singular vectors shown in figure A1 are related to the gyrotrons. Also, we note that the neutral beam injectors have a broad influence on the $q$ profile while the gyrotron launchers have a more localized effect on the $q$ profile, which is consistent with the noninductive current source profiles shown in figure 1(f).

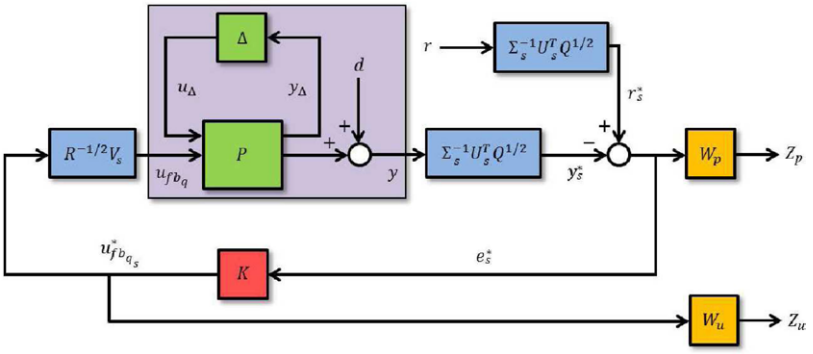


**Figure A3.** Schematic of safety factor profile control problem formulation. The uncertain state-space system (A.1) is shown in the light purple box. The blocks $\Sigma_s^{-1}U_s^TQ^{1/2}$ and $R^{-1/2}V_s$ are used to obtain a decoupled relationship between the outputs and inputs of the system, which allows us to design a square feedback controller $K \in \mathbb{R}^{k_s \times k_s}$. The outputs of the closed-loop system are defined as $Z_p = W_p(s)e_s^* \in \mathbb{R}^{k_s}$ and $Z_u = W_u(s)u^*_{\mathrm{fb}_{q_s}} \in \mathbb{R}^{k_s}$, where $W_p \in \mathbb{R}^{k_s \times k_s}$ and $W_u \in \mathbb{R}^{k_s \times k_s}$ are frequency-dependent weight functions.

### *A.3. Safety factor profile feedback control algorithm synthesis*

We aim to achieve the feedback control objectives by controlling the relevant input–output channels of the system (A.1), which is equivalent to the system (44) and (45). This control problem formulation is shown in figure A3, where $K$ is the feedback controller and $W_p$ and $W_u$ are frequency-dependent weight functions that are used to optimize the closed-loop performance of the system. The *nominal performance* condition of the closed-loop system is expressed as

$$\begin{bmatrix} Z_p \\ Z_u \end{bmatrix} = \begin{bmatrix} W_p\, S_{\mathrm{DC}_O} & -W_p\, S_{\mathrm{DC}_O} \\ W_u K S_{\mathrm{DC}_O} & -W_u K S_{\mathrm{DC}_O} \end{bmatrix} \begin{bmatrix} r_s^* \\ d_s^* \end{bmatrix} \triangleq T_{zw} \begin{bmatrix} r_s^* \\ d_s^* \end{bmatrix}, \quad \text{(A.7)}$$

which describes how the external system inputs $r_s^*$ and $d_s^*$ affect the system outputs $Z_p = W_p e_s^*$ and $Z_u = W_u u^*_{\mathrm{fb}_{q_s}}$, where $S_{\mathrm{DC}_O} = (I_{k_s} + \Sigma_s^{-1}U_s^TQ^{1/2}P_{22}R^{-1/2}V_sK)^{-1}$, $d_s^* = \Sigma_s^{-1}U_s^TQ^{1/2}d$ and $I_{k_s}$ is a $k_s \times k_s$ identity matrix. The function $S_{\mathrm{DC}_O}$ is the closed-loop transfer function between the input $r_s^*$ and the output $e_s^*$, and the function $KS_{\mathrm{DC}_O}$ is the closed-loop transfer function between the input $r_s^*$ and the output $u^*_{\mathrm{fb}_{q_s}}$. The feedback control objectives are to (i) maintain a small tracking error for any external reference input and (ii) reject the effects of any external disturbance input while using as little feedback control effort as possible as discussed in section 6.3. Therefore, the control problem is formulated as shown in (47). By examining the definition of the transfer function $S_{\mathrm{DC}_O}$, we see that the minimization in (47) is based on the transfer function $\Sigma_s^{-1}U_s^TQ^{1/2}P_{22}R^{-1/2}V_s$, which represents the nominal transfer function $P_{22}$ projected onto both the input and output basis that are determined by the SVD analysis shown in appendix A.2. The safety factor profile feedback controller $K$ found by solving the control problem is written in state-space form as

$$\begin{aligned} \dot{x}_{\mathrm{fb}_q} &= A^*_{\mathrm{fb}_q} x_{\mathrm{fb}_q} + B^*_{\mathrm{fb}_q} e_s^*, \\ u^*_{\mathrm{fb}_{q_s}} &= C^*_{\mathrm{fb}_q} x_{\mathrm{fb}_q} + D^*_{\mathrm{fb}_q} e_s^*, \end{aligned}$$

where the vector $x_{\mathrm{fb}_q} \in \mathbb{R}^{n_{\mathrm{fb}_q}}$ is the internal controller states, $A^*_{\mathrm{fb}_q} \in \mathbb{R}^{n_{\mathrm{fb}_q} \times n_{\mathrm{fb}_q}}$, $B^*_{\mathrm{fb}_q} \in \mathbb{R}^{n_{\mathrm{fb}_q} \times k_s}$, $C^*_{\mathrm{fb}_q} \in \mathbb{R}^{k_s \times n_{\mathrm{fb}_q}}$ and $D^*_{\mathrm{fb}_q} \in \mathbb{R}^{k_s \times k_s}$

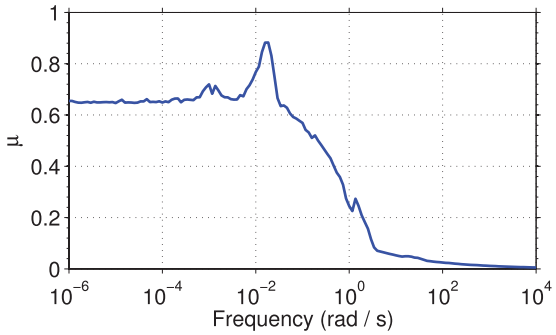


**Figure A4.** Structured singular value versus frequency. The closed-loop system is robustly stable for all allowable perturbations if and only if $\mu(N_{11}(j\omega)) < 1, \forall\, \omega$ [63].

are the controller system matrices and $n_{\mathrm{fb}_q}$ is the number of controller states. Equivalently, the feedback controller can be written in terms of the tracking error $e$ and control input $u_{\mathrm{fb}_q}$ as given in (48), where

$$\begin{aligned} A_{\mathrm{fb}_q} &= A^*_{\mathrm{fb}_q}, \\ B_{\mathrm{fb}_q} &= B^*_{\mathrm{fb}_q}\Sigma_s^{-1}U_s^TQ^{1/2}, \\ C_{\mathrm{fb}_q} &= R^{-1/2}V_sC^*_{\mathrm{fb}_q}, \\ D_{\mathrm{fb}_q} &= R^{-1/2}V_sD^*_{\mathrm{fb}_q}\Sigma_s^{-1}U_s^TQ^{1/2}. \end{aligned}$$

The *robust stability* of the closed-loop system is analyzed by exploiting the block-diagonal structure of the uncertainty matrix, i.e. $\Delta = \mathrm{diag}\{\delta_{T_e}, \delta_{n_e}\}$, which allows us to compute the structured singular value [63]

$$\mu(N_{11}(j\omega)) = \frac{1}{\min\{k_m | \det(I - k_m N_{11}\Delta) = 0\}},$$

where $N_{11} = P_{11} - P_{12}R^{-1/2}V_sKS_{\mathrm{DC}_O}\Sigma_s^{-1}U_s^TQ^{1/2}P_{21}$ is the closed-loop transfer function between the signals $y_\Delta$ and $u_\Delta$ shown in figure A3. Figure A4 shows a plot of $\mu$ versus frequency, and as can be seen from the figure, $\mu$ is less than one for all frequencies, which implies that the closed-loop system is robustly stabilized by the feedback controller [63], i.e. the closed-loop system is stable for the ranges of the kinetic plasma parameters shown in figure 10.

## References


[1] Hawryluk R J *et al* 1980 An empirical approach to Tokamak transport *Physics of Plasmas Close to Thermonuclear Conditions* vol 1 ed B Coppi *et al* (Oxford: Pergamon) pp 19–46
[2] St John H E *et al* 1996 *Proc. 15th Int. Conf. on Plasma Physics and Controlled Nuclear Fusion Research* (*Seville, Spain*, *1994*)vol 3 (Vienna: IAEA) p 603
[3] Crotinger J *et al* 1997 *Technical Report* UCRL-ID-126284 LLNL
[4] Pereverzev G V *et al* 2002 ASTRA: automated system for transport analysis in a tokamak *Technical Report* IPP Report 5/98
[5] Kim S H *et al* 2009 *Plasma Phys. Control. Fusion* **51** 105007
[6] Favez J Y *et al* 2002 *Plasma Phys. Control. Fusion* **44** 171
[7] Basiuk V *et al* 2003 *Nucl. Fusion* **43** 822
[8] Besseghir K *et al* 2013 *Plasma Phys. Control. Fusion* **55** 125012
[9] Besseghir K 2013 Free-boundary simulations of ITER advanced scenarios *PhD Thesis* École Polytechnique Fédérale de Lausanne
[10] Park J M *et al* 2010 Experiment and modeling of ITER demonstration discharges in the DIII-D Tokamak *Proc. 23rd Int. Conf. on Fusion Energy (Daejeon, Korea*, *2010)* paper EXC/P2-05
[11] Taylor T *et al* 1997 *Plasma Phys. Control. Fusion* **39** B47
[12] Peeters A G 2000 *Plasma Phys. Control. Fusion* **42** B231
[13] Gormezano C *et al* 2007 *Nucl. Fusion* **47** S285
[14] Waltz R E *et al* 1995 *Phys. Plasmas* **2** 2408
[15] Petty C C *et al* 1998 *Phys. Plasmas* **5** 1695
[16] Ferron J *et al* 2005 *Phys. Plasmas* **12** 056126
[17] Hender T C *et al* 2007 *Nucl. Fusion* **47** S128
[18] Politzer P A and Porter G D 1990 *Nucl. Fusion* **30** 1605
[19] Luce T C *et al* 1999 *Phys. Rev. Lett.* **83** 4550
[20] Sauter O *et al* 1997 *Phys. Plasmas* **4** 1654
[21] Ferron J *et al* 2011 *Nucl. Fusion* **51** 063026
[22] Laborde L *et al* 2005 *Plasma Phys. Control. Fusion* **47** 155
[23] Moreau D *et al* 2003 *Nucl. Fusion* **43** 870
[24] Moreau D *et al* 2008 *Nucl. Fusion* **48** 106001
[25] Ferron J *et al* 2006 *Nucl. Fusion* **46** L13
[26] Moreau D *et al* 2011 *Nucl. Fusion* **51** 063009
[27] Moreau D *et al* 2012 Integrated magnetic and kinetic control of advanced Tokamak scenarios based on data-driven models *24th IAEA Fusion Energy Conf. (San Diego, CA, USA)* paper ITR/P1-20
[28] Barton J E *et al* 2012 First-principles model-based closed-loop control of the current profile dynamic evolution on DIII-D *24th IAEA Fusion Energy Conf. (San Diego, CA, USA)* paper EX/P2-09
[29] Barton J E *et al* 2012 *Nucl. Fusion* **52** 123018
[30] Boyer M D *et al* 2013 *Plasma Phys. Control. Fusion* **55** 105007
[31] Boyer M D *et al* 2014 *IEEE Trans. Control Syst. Technol.* **22** 1725
[32] Shi W *et al* 2012 Multivariable robust control of the plasma rotational transform profile for advanced Tokamak scenarios in DIII-D *American Control Conf. Proc. (Montreal, QC, Canada)* pp 5037–42
[33] Wehner W *et al* 2012 Optimal feedback control of the poloidal magnetic flux profile in the DIII-D Tokamak based on identified plasma response models *American Control Conf. Proc. (Montreal, QC, Canada)* pp 5049–54
[34] Shi W *et al* 2012 A two-time-scale model-based combined magnetic and kinetic control system for advanced Tokamak scenarios on DIII-D *51st IEEE Conf. on Decision and Control Proc. (Maui, HI, USA)* pp 4347–52
[35] Moreau D *et al* 2013 *Nucl. Fusion* **53** 063020
[36] Shi W *et al* 2013 PTRANSP simulation and experimental test of a robust current profile and $\beta_N$ controller for off-axis current-drive scenarios in the DIII-D Tokamak *American Control Conf. Proc. (Washington DC, USA)* pp 1225–30
[37] Barana O *et al* 2007 *Plasma Phys. Control. Fusion* **49** 947
[38] Wijnands T *et al* 1997 *Nucl. Fusion* **37** 777
[39] Suzuki T *et al* 2005 Recent RF experiments and application of RF waves to real-time control of safety factor profile in JT-60U *AIP Conf. Proc. (Park City, UT, USA)* pp 279–86
[40] Suzuki T *et al* 2008 *Nucl. Fusion* **48** 045002
[41] Kim S H and Lister J B 2012 *Nucl. Fusion* **52** 074002
[42] Witrant E *et al* 2007 *Plasma Phys. Control. Fusion* **49** 1075
[43] Ou Y *et al* 2007 *Fusion Eng. Des.* **82** 1153
[44] Felici F *et al* 2011 *Nucl. Fusion* **51** 083052
[45] Hinton F and Hazeltine R 1976 *Rev. Mod. Phys.* **48** 239
[46] Blum J 1989 *Numerical Simulation and Optimal Control in Plasma Physics: with Applications to Tokamaks* (Paris: Wiley)
[47] Artaud J F *et al* 2005 *32nd EPS Conf. on Plasma Physics* (*Tarragona, Spain*) vol 29C p P–1.035
[48] Barton J E *et al* 2014 Nonlinear physics-model-based actuator trajectory optimization for advanced scenario planning in the DIII-D Tokamak *19th IFAC World Congress (Cape Town, South Africa)* pp 671–6
[49] Barton J E *et al* 2015 *Nucl. Fusion* **55** 093005
[50] Ou Y, Xu C and Schuster E 2010 *IEEE Trans. Plasma Sci.* **38** 375
[51] Ou Y, Xu C and Schuster E 2011 *IEEE Trans. Control Syst. Technol.* **19** 432
[52] Xu C, Ou Y and Schuster E 2011 *Automatica* **47** 418
[53] Ou Y *et al* 2011 *Control Eng. Pract.* **19** 22
[54] Gaye O *et al* 2011 Sliding mode stabilization of the current profile in Tokamak plasmas *50th IEEE Conf. on Decision and Control (Orlando, FL, USA)* pp 2638–43
[55] Gahlawat A *et al* 2012 Bootstrap current optimization in Tokamaks using sum-of-squares polynomials *51st IEEE Conf. on Decision and Control (Maui, HI, USA)* pp 4359–65
[56] Argomedo F *et al* 2013 *Nucl. Fusion* **53** 033005
[57] Vu N M T, Nouailletas R, Lefevre L and Bremond S 2013 An IDA-PBC approach for the control of 1D plasma profile in Tokamaks *52nd IEEE Conf. on Decision and Control (Florence, Italy)* pp 4176–81
[58] Hively L M 1977 *Nucl. Fusion* **17** 873
[59] Sauter O *et al* 1999 *Phys. Plasmas* **6** 2834
[60] Sauter O *et al* 2002 *Phys. Plasmas* **9** 5140
[61] ITER Physics Basis 1999 *Nucl. Fusion* **39** 2137
[62] Goldston R J 1984 *Plasma Phys. Control. Fusion* **26** 87
[63] Skogestad S and Postlethwaite I 2005 *Multivariable Feedback Control Analysis and Design* (New York: Wiley)
[64] Barton J E 2015 Physics-model-based optimization and feedback control of the current profile dynamics in fusion tokamak reactors *PhD Thesis* Lehigh University
[65] Schiesser W 1991 *The Numerical Method of Lines: Integration of Partial Differential Equations* (San Diego: Academic)
[66] Zaccarian L and Teel A R 2011 *Modern Anti-windup Synthesis: Control Augmentation for Actuator Saturation* (Princeton, NJ: Princeton University Press)
[67] Ferron J *et al* 1998 *Nucl. Fusion* **38** 1055
[68] Boyer M D 2014 Nonlinear burn condition and kinetic profile control in Tokamak fusion reactors *PhD Thesis* Lehigh University
[69] Baylor L *et al* 2007 *Nucl. Fusion* **47** 443
[70] Barton J E *et al* 2013 Physics-based control-oriented modeling of the safety factor profile dynamics in high performance Tokamak plasmas *52nd IEEE Conf. on Decision and Control (Florence, Italy)* pp 4182–7

[71] Barton J E *et al* 2014 Physics-model-based control of the plasma current profile dynamics for the development and sustainment of advanced scenarios in DIII-D *25th IAEA Fusion Energy Conf. (Saint Petersburg, Russia)* paper PPC/P2-32
[72] Barton J E *et al* 2014 Experimental and simulation testing of physics-model- based safety factor profile and internal energy feedback controllers in DIII-D advanced Tokamak scenarios *19th IFAC World Congress (Cape Town, South Africa)* pp 5223–8
[73] Boyer M D *et al* 2014 Simultaneous boundary and distributed feedback control of the current profile in H-mode discharges on DIII-D *19th IFAC World Congress (Cape Town, South Africa)* pp 1568–73
[74] Wehner W *et al* 2014 First-principles-driven model-based control of the poloidal magnetic flux profile at the DIII-D Tokamak *19th IFAC World Congress (Cape Town, South Africa)* pp 10319–24
[75] Shi W *et al* 2013 First-principles driven control of the rotational transform profile in high performance discharges in the DIII-D Tokamak *52nd IEEE Conf. on Decision and Control* (*Florence, Italy*) pp 4170–5
[76] Packard A 1988 Whats new with $\mu$: structured uncertainty in multivariable control *PhD Thesis* University of California, Berkeley
[77] Edmunds J and Kouvaritakis B 1979 *Int. J. Control* **29** 787
[78] Golub G and Loan C F V 1996 *Matrix Computations* 3rd edn (Baltimore: Johns Hopkins University Press)